Aerospace Science and Technology 155 (2024) 109596

Contents lists available at ScienceDirect

Aerospace Science and Technology

journal homepage: www.elsevier.com/locate/aescte

Geometric extended state observer on TSE(3) with fast finite-time stability: Theory and validation on a multi-rotor vehicle

Ningshan Wang [a], Reza Hamrah [b], Amit K. Sanyal [c,*], Mark N. Glauser [c]

[a] Department of Mechanical Engineering, University of Michigan, United States of America
[b] Blue Origin Enterprises, L.P., United States of America
[c] Department of Mechanical & Aerospace Engineering, Syracuse University, United States of America

ARTICLE INFO

Communicated by Jayaram Sanjay

Keywords:
Geometric mechanics
Extended state observer
Fast finite-time stability
Unmanned aerial vehicle

ABSTRACT

This article presents an extended state observer for a vehicle modeled as a rigid body in three-dimensional translational and rotational motions. The extended state observer is applicable to a multi-rotor aerial vehicle with a fixed plane of rotors, modeled as an under-actuated system on the state-space TSE(3), the tangent bundle of the six-dimensional Lie group SE(3). This state-space representation globally represents rigid body motions without singularities. The extended state observer is designed to estimate the resultant external disturbance force and disturbance torque acting on the vehicle. It guarantees stable convergence of disturbance estimation errors in finite time when the disturbances are constant, and finite time convergence to a bounded neighborhood of zero errors for time-varying disturbances. This extended state observer design is based on a Hölder-continuous fast finite time stable differentiator that is similar to the super-twisting algorithm, to obtain fast convergence. Numerical simulations are conducted to validate the proposed extended state observer. The proposed extended state observer is compared with other existing research to show its advantages. A set of experimental results implementing disturbance rejection control using feedback of disturbance estimates from this extended state observer is also presented.

1. Introduction

Multi-rotor unmanned aerial vehicles (UAVs) are increasingly being used in various applications, such as security and monitoring, infrastructure inspection, agriculture, wildland management, package delivery, and remote sensing. However, these UAVs are frequently exposed to dynamic uncertainties and disturbances caused by turbulence induced by winds and airflow around structures or regions. Therefore, it is crucial to ensure robust flight control performance in such challenging environments, with guaranteed stability margins even in the presence of dynamic disturbances and uncertainties. This is made more challenging by the fact that the state space of rigid body motions is the tangent bundle of the Lie group SE(3), which is not contractible. Therefore, continuous control or state estimation schemes cannot be globally convergent in this state space, as explained in [7].

Recent research articles on multi-rotor UAV tracking control have used various methods to tackle the adverse effects of disturbances and uncertainties during flight. Torrente et al. [37] used Gaussian processes to complement the nominal dynamics of the multi-rotor in a model predictive control (MPC) pipeline. Hanover et al. [14] used an explicit scheme to discretize the dynamics for a nonlinear MPC solved by optimization. Bangura and Mahony [1] used the propeller aerodynamics as a direct feedforward term on the desired thrust to re-regulate the thrust command of the rotors. Craig et al. [10] attached a set of pitot tubes onto the multi-rotor aircraft to directly sense the aircraft's airspeed. With the knowledge of propeller aerodynamic characteristics, the airspeed was then utilized to obtain the disturbance forces and torques as feedforward terms to enhance control performance. Bisheban and Lee [5] implemented artificial neural networks to obtain disturbance forces and torques with the kinematics information of the aircraft, and then used the baseline control scheme based on the article by Lee et al. [20] in their tracking control scheme design. The methods used in these research articles either need high computational efforts [37,14,5], or they require precise modeling of the aerodynamic characteristics of the multi-rotor propellers [1,10], to obtain satisfactory control performance in the presence of disturbances.

* Corresponding author.
E-mail addresses: nswang@umich.edu (N. Wang), rhamrah@blueorigin.com (R. Hamrah), aksanyal@syr.edu (A.K. Sanyal), mglauser@syr.edu (M.N. Glauser).

https://doi.org/10.1016/j.ast.2024.109596
Received 26 April 2024; Received in revised form 31 July 2024; Accepted 14 September 2024
Available online 20 September 2024

Extended state observers, along with disturbance observers and unknown input observers, are commonly used in association with the robust control technique known as *active disturbance rejection control* (ADRC), which can be traced back to the dissertation by Hartlieb [16]. In an ADRC scheme, estimates of unknown disturbance inputs from a disturbance observer (DO) or an extended state observer (ESO) are first obtained and then utilized in the control design to reject the disturbance. These observers can also be used to estimate parameters in a disturbance model. For example, Jia et al. [18] employed the disturbance model obtained by Faessler et al. [12], and then estimated the drag coefficient as a parameter. This disturbance model was also employed by Moeini et al. [26]. See, for example, Huang et al. [17], Shao et al. [36], Mechali et al. [24], Cui et al. [11] on applications of ESO schemes, and Chen [9], Liu et al. [22], Bhale et al. [2], Sanyal [33] on applications of DO schemes for ADRC of spatial motions of vehicles in three dimensions.

There are several methods to ensure the local stability of ESO/DO designs used for multi-rotor tracking control. The linear ESO by Shao et al. [36] is locally asymptotically stable (AS), when its state-space is near the origin. Mechali et al. [24] used the concept of geometric homogeneity [32] to obtain an ESO that is locally finite-time stable. A similar method was proposed in the ESO design by Guo and Zhao [13]. The Lyapunov functions/candidates used in the ESO stability analysis by Mechali et al. [24] and Guo and Zhao [13] are based on [32], and are implicit. Jia et al. [18], Moeini et al. [26] and Liu et al. [22] used variants of the DO proposed by Chen [9]. Another approach is to use the super-twisting algorithm (STA) Moreno and Osorio [27] to design ESO. Xia et al. [43] use this method in ESO design for spacecraft attitude control, and Cui et al. [11] designed an adaptive super-twisting ESO for an ADRC scheme applied to a multi-rotor vehicle.

In much of the prior literature for multi-rotor UAV attitude control with ESO/DO for disturbance torque estimation and rejection in rotational dynamics, the attitude kinematics of the ESO/DO are either based on local linearization or represented using local coordinates (like Euler angles) or using quaternions. Local coordinate representations can have singularity issues (e.g., gimbal lock with Euler angles), while continuous quaternion feedback causes instability due to unwinding [4,7]. In situations where a vehicle has to carry out aggressive maneuvers, as in rapid collision avoidance for example, disturbance estimation and rejection using such schemes may not be reliable for stable control of the vehicle.

This article presents an ESO on the state space TSE(3) for multi-rotor vehicles to provide reliable disturbance estimation under complex and challenging aerodynamic environments. The ESO on TSE(3) estimates the disturbance forces and torques during the flight of a vehicle for both translational and rotational motions. The proposed ESO is fast finite-time stable (FFTS), abbreviated as FFTS-ESO. This FFTS-ESO design is based on a novel Hölder-continuous fast finite-time stable differentiator (HC-FFTSD). We carry out several sets of numerical simulations to show the validity of the proposed FFTS-ESO. Moreover, the proposed FFTS-ESO is compared with the extended state observer by Shao et al. [36] and the disturbance observer by Liu et al. [22] in the conducted simulations to show the advantages of the proposed method. A set of experimental results implementing a disturbance rejection mechanism using feedback of disturbance estimates from the FFTS-ESO is also presented. In the experiment, we hover the vehicle in front of the turbulent flows generated by a fan array wind tunnel (FAWT). We obtain statistical information from the hot-wire measurements on the turbulent incoming flows. We observe the pose of the vehicle to evaluate its flight control performance.

We highlight some unique contributions of this article.

- The proposed ESO is the major contribution of this article. The pose of the multi-rotor is represented directly on the Lie group of rigid body transformations, the special Euclidean group SE(3). Unlike the ESO and DO designs reported by Mechali et al. [24], Shao et al. [36], Liang et al. [21], and Cui et al. [11], who used Euler angles or quaternions for attitude representation or did not include attitude kinematics, like the DO by Bhale et al. [2] in disturbance torque estimation, the pose of the vehicle in this article is represented in SE(3) to avoid kinematic singularities. We do not use local coordinates (like Euler angles) or (dual) quaternions for pose representation so that we avoid singularities due to local coordinate representations or quaternion unwinding, as reported by Bhat and Bernstein [4], and Chaturvedi et al. [7]. To the best of the author's knowledge, there is no existing publication on aircraft disturbance observation using ESO with pose representation on SE(3).
- The proposed FFTS-ESO is based on the HC-FFTSD. The commonly used geometric homogeneity method in [32,13,23,41,42], cannot provide a straightforward (or explicit) Lyapunov function to prove the finite-time stability of the scheme. The (implicit) form of their Lyapunov functions is given by Rosier [32]. This implicit Lyapunov function complicates the robustness analysis under measurement noise and time-varying disturbances when that analysis is essential for an ESO designed for disturbance estimation in ADRC schemes. We propose HC-FFTSD as an approach inspired by the (STA) by Moreno and Osorio [27], Vidal et al. [38] of sliding-mode control (SMC). This approach gives a straightforward design of a strict Lyapunov function, which is explicit, and therefore avoids the weakness mentioned above.
- Based on the HC-FFTSD, the FFTS-ESO schemes obtained here are both FFTS and Hölder-continuous, unlike the common STA and other FTS schemes that use discontinuous methods like terminal sliding-mode. Therefore, they avoid the potentially harmful chattering phenomenon [35], while maintaining FTS convergence.
- Using explicit Lyapunov functions in the stability analysis, we present proof of the robustness of the proposed FFTS-ESO under time-varying disturbing forces and torques.

The remainder of the article is as follows. Section 2 presents some preliminary results that are needed to obtain sufficient conditions for the stability of the ESO and ADRC schemes. HC-FFTSD is presented, along with its stability and robustness analysis in Section 3. Section 4 defines and describes the state-space on TSE(3) with details. Based on the definition, the ESO design problem on TSE(3) is formulated. Section 5 describes the detailed FFTS-ESO design, which is based on the differentiator design in Section 3. Numerical simulations are conducted in Section 6. Section 7 describes the conducted UAV flight experiment with the UAV exposed to the disturbances generated by the FAWT in detail. We conclude the paper, in Section 8, by summarizing the results and highlighting directions for forthcoming research.

2. Preliminaries

The statements and definitions in this section are used in the technical results obtained in later sections. The statements given here give the conditions under which a continuous time system is finite-time stable, fast finite-time stable, and practically finite-time stable using Lyapunov analysis, and the last statement is used in developing the main result.

Lemma 1 *(Finite-time stable).* [3] *Consider the following system of differential equations,*

$$\dot{x}(t) = f(x(t)),\ f(0) = 0,\ x(0) = x_0, \tag{1}$$

where $f : \mathcal{D} \to \mathbb{R}^n$ is continuous on an open neighborhood $\mathcal{D} \subset \mathbb{R}^n$ of the origin, and let there be a continuous and differentiable function $V(x(t))$ that is positive definite. Let the time derivative of $V(x)$ satisfy the following inequality:

$$\dot{V} \leq -\lambda V^{\alpha}, \tag{2}$$

where $x(t) \in \mathcal{D}\backslash\{0\}$, $\lambda > 0$, $\alpha \in]0,1[$. Then the system (1) is FTS at the origin, which means $\forall x_0 \in \mathcal{D}$, x can reach the origin in finite time. Moreover, the settling time T, the time needed to reach the origin, satisfies

$$T \leq \frac{V^{1-\alpha}(x_0)}{\lambda(1-\alpha)}. \tag{3}$$

Lemma 2 *(Fast finite-time stable).* [45], [44] *Consider the system (1) and let there be a continuous and differentiable function $V(x(t))$ that is positive definite. Let the time derivative of $V(x)$ satisfy the following inequality:*

$$\dot{V} \leq -\lambda_1 V - \lambda_2 V^{\alpha}, \tag{4}$$

where $x(t) \in \mathcal{D}\backslash\{0\}$, $\lambda_1, \lambda_2 > 0$, $\alpha \in]0,1[$. Then the system (1) is FFTS at the origin and the settling time T satisfies:

$$T \leq \frac{1}{\lambda_1(1-\alpha)} \ln \frac{\lambda_1 V^{1-\alpha}(x_0) + \lambda_2}{\lambda_2}. \tag{5}$$

Lemma 3 *(Practically finite-time stable).* [45,46,44] *Consider the system (1) and let there be a continuous and differentiable function $V(x)$ that is positive definite. Let the time derivative of $V(x)$ satisfy the following inequality:*

$$\dot{V} \leq -\lambda_1 V - \lambda_2 V^{\alpha} + \eta, \tag{6}$$

where $x(t) \in \mathcal{D}\backslash\{0\}$, $\lambda_1, \lambda_2 > 0$, and $\alpha \in]0,1[$. Then the system (1) is practical finite-time stable (PFTS) at the origin, which means that the solution of (1) will converge to the following set in finite time

$$\left\{ x \,\middle|\, V(x) \leq \min\left\{ \frac{\eta}{(1-\theta_0)\lambda_1}, \left(\frac{\eta}{(1-\theta_0)\lambda_2} \right)^{\frac{1}{\alpha}} \right\} \right\},$$

where $0 < \theta_0 < 1$. The settling time T is bounded above as follows:

$$T \leq \max\left\{ t_0 + \frac{1}{\theta_0\lambda_1(1-\alpha)} \ln \frac{\theta_0\lambda_1 V^{1-\alpha}(x_0) + \lambda_2}{\lambda_2}, t_0 + \frac{1}{\lambda_1(1-\alpha)} \ln \frac{\lambda_1 V^{1-\alpha}(x_0) + \theta_0\lambda_2}{\theta_0\lambda_2} \right\}.$$

Lemma 4. [15] *Let x and y be non-negative real numbers and let $p \in]1,2[$. Then*

$$x^{\frac{1}{p}} + y^{\frac{1}{p}} \geq (x+y)^{\frac{1}{p}}. \tag{7}$$

Moreover, the above inequality is a strict inequality if both x and y are non-zero.

Definition 1. Define $H : \mathbb{R}^3 \times \mathbb{R} \to \mathrm{Sym}(3)$, the space of symmetric 3×3 matrices, as follows:

$$H(x,k) := I - \frac{2k}{x^{\mathrm{T}}x} x x^{\mathrm{T}}. \tag{8}$$

3. Hölder-continuous fast finite-time stable differentiator (HC-FFTSD)

In this section, we design the error dynamics for the proposed ESO in Section 5 in the form of an HC-FFTSD. We analyze the stability and robustness of the proposed HC-FFTSD in this section, to support the development of the ESO design in Section 5. Theorem 1 gives the proposed HC-FFTSD with its stability properties. Corollary 1 describes the convergence performance of the differentiator under external perturbations. In the analysis that follows, $e_1 \in \mathbb{R}^n$ stands for the measurement estimation error and $e_2 \in \mathbb{R}^n$ stands for the disturbance estimation error in the ESO error dynamics, respectively. In this section and the remainder of this paper, we denote the minimum and maximum eigenvalues of a matrix by $\lambda_{\min}(\cdot)$ and $\lambda_{\max}(\cdot)$, respectively.

Theorem 1. *Let $p \in]1,2[$ and $k_3 > 0$. Define $\phi_1(\cdot) : \mathbb{R}^n \to \mathbb{R}^n$ and $\phi_2(\cdot) : \mathbb{R}^n \to \mathbb{R}^n$ as follows:*

$$\begin{aligned} \phi_1(e_1) &= k_3 e_1 + (e_1^{\mathrm{T}} e_1)^{\frac{1-p}{3p-2}} e_1, \\ \phi_2(e_1) &= k_3^2 e_1 + \frac{2k_3(2p-1)}{3p-2} (e_1^{\mathrm{T}} e_1)^{\frac{1-p}{3p-2}} e_1 + \frac{p}{3p-2} (e_1^{\mathrm{T}} e_1)^{\frac{2(1-p)}{3p-2}} e_1, \end{aligned} \tag{9}$$

where $e_1, e_2 \in \mathbb{R}^n$. Define the differentiator gains $k_1, k_2 > 0$ and $\mathcal{A}^* \in \mathbb{R}^{2\times 2}$, as:

$$\mathcal{A}^* = \begin{bmatrix} -k_1 & 1 \\ -k_2 & 0 \end{bmatrix}, \tag{10}$$

which makes $\mathcal{A}^*$ a Hurwitz matrix. Thereafter, the differentiator design:

$$\begin{aligned} \dot{e}_1 &= -k_1\phi_1(e_1) + e_2, \\ \dot{e}_2 &= -k_2\phi_2(e_1), \end{aligned} \tag{11}$$

ensures that e_1, e_2 converge to the origin in a fast finite-time stable manner.

Proof. The proof of Theorem 1 is based on Theorem 1 by Vidal et al. [38], Moreno et al. [28] and Theorem 1 by Moreno and Osorio [27]. Two properties of ϕ_1 and ϕ_2 are provided as follows.

Property 1 (P1): The Jacobian of $\phi_1(e_1)$, denoted $\phi_1'(e_1)$, is given as follows:

$$\phi_1'(e_1) = \frac{\mathrm{d}\phi_1(e_1)}{\mathrm{d}e_1} = k_3 I + (e_1^{\mathrm{T}} e_1)^{\frac{1-p}{3p-2}} \left[I - \frac{2(p-1)}{3p-2} \frac{e_1 e_1^{\mathrm{T}}}{e_1^{\mathrm{T}} e_1} \right], \tag{12}$$

so that the following identity holds:

$$\phi_2(e_1) = \phi_1'(e_1)\phi_1(e_1) \tag{13}$$

Property 2 (P2): ϕ_1' is a positive definite matrix, which means $\forall w \in \mathbb{R}^n, e_1 \in \mathbb{R}^n$,

$$\lambda_{\min}\{\phi_1'(e_1)\}||w||^2 \le w^{\mathrm{T}}\phi_1'(e_1)w \le \lambda_{\max}\{\phi_1'(e_1)\}||w||^2, \tag{14}$$

where the maximum and minimum eigenvalues of $\phi_1'(e_1)$ in (14) are as given below:

$$\lambda_{\max}\{\phi_1'(e_1)\} = k_3 + (e_1^{\mathrm{T}} e_1)^{\frac{1-p}{3p-2}}, \tag{15}$$

$$\lambda_{\min}\{\phi_1'(e_1)\} = k_3 + (e_1^{\mathrm{T}} e_1)^{\frac{1-p}{3p-2}} \frac{p}{3p-2}. \tag{16}$$

From Theorem 5.5 by Chen [8], we know that for a Hurwitz matrix $\mathcal{A}^*$ as in (10), $\forall \mathcal{Q}^* \in \mathbb{R}^{2\times 2}$ where $\mathcal{Q}^* \succ 0$, the Lyapunov equation:

$$(\mathcal{A}^*)^{\mathrm{T}}\mathcal{P}^* + \mathcal{P}^*\mathcal{A}^* = -\mathcal{Q}^*, \tag{17}$$

has a unique solution $\mathcal{P}^* \succ 0$. Express the positive definite matrices $\mathcal{P}^*$ and $\mathcal{Q}^*$ in components as follows:

$$\mathcal{P}^* = \begin{bmatrix} p_{11} & p_{12} \\ p_{12} & p_{22} \end{bmatrix}, \ \mathcal{Q}^* = \begin{bmatrix} q_{11} & q_{12} \\ q_{12} & q_{22} \end{bmatrix}.$$

As $\mathcal{P}^*$ is the solution to (17), $\mathcal{A}^*$, $\mathcal{P}^*$ and $\mathcal{Q}^*$ can be augmented to $\mathcal{A}, \mathcal{P}, \mathcal{Q} \in \mathbb{R}^{2n\times 2n}$, as follows:

$$\mathcal{A} = \begin{bmatrix} -k_1 I & I \\ -k_2 I & 0 \end{bmatrix}, \mathcal{P} = \begin{bmatrix} p_{11} I & p_{12} I \\ p_{12} I & p_{22} I \end{bmatrix}, \mathcal{Q} = \begin{bmatrix} q_{11} I & q_{12} I \\ q_{12} I & q_{22} I \end{bmatrix}.$$

The augmented matrices $\mathcal{A}, \mathcal{P}, \mathcal{Q}$ defined above also satisfy a Lyapunov equation as given below:

$$\mathcal{A}^{\mathrm{T}}\mathcal{P} + \mathcal{P}\mathcal{A} = -\mathcal{Q}. \tag{18}$$

Further, the eigenvalues of $\mathcal{P}$ and $\mathcal{P}^*$, are related such that $\lambda_{\min}\{\mathcal{P}^*\} = \lambda_{\min}\{\mathcal{P}\}$, and $\lambda_{\max}\{\mathcal{P}^*\} = \lambda_{\max}\{\mathcal{P}\}$. Similar relations hold for $\mathcal{Q}$ and $\mathcal{Q}^*$. Therefore, as $\mathcal{P}$ is the solution to (18), we consider the following Lyapunov candidate:

$$V(e_1, e_2) = \zeta^{\mathrm{T}}\mathcal{P}\zeta, \tag{19}$$

where $\zeta \in \mathbb{R}^{2n}$ is defined as $\zeta := [\phi_1^{\mathrm{T}}(e_1), e_2^{\mathrm{T}}]^{\mathrm{T}}$ and $\mathcal{P}$ is the augmented $\mathcal{P}^*$, which is the unique solution of (17) for a given $\mathcal{Q}^* \succ 0$. The upper and lower bounds of the Lyapunov candidate V in (19) are as given below:

$$\lambda_{\min}\{\mathcal{P}\}\,\|\zeta\|^2 \le V(e_1, e_2) \le \lambda_{\max}\{\mathcal{P}\}\,\|\zeta\|^2, \tag{20}$$

where $\|\zeta\|^2$ is expressed as follows:

$$\begin{aligned} \|\zeta\|^2 &= \phi_1^{\mathrm{T}}(e_1)\phi_1(e_1) + e_2^{\mathrm{T}}e_2 \\ &= k_3^2 e_1^{\mathrm{T}}e_1 + 2k_3(e_1^{\mathrm{T}}e_1)^{\frac{2p-1}{3p-2}} + (e_1^{\mathrm{T}}e_1)^{\frac{p}{3p-2}} + e_2^{\mathrm{T}}e_2. \end{aligned} \tag{21}$$

From (20) and (21), we obtain the following inequalities:

$$\lambda_{\min}\{\mathcal{P}\}(e_1^{\mathrm{T}}e_1)^{\frac{p}{3p-2}} \le \lambda_{\min}\{\mathcal{P}\}\,\|\zeta\|^2 \le V(e_1, e_2), \tag{22}$$

$$k_3^2\lambda_{\min}\{\mathcal{P}\}\,e_1^{\mathrm{T}}e_1 \le \lambda_{\min}\{\mathcal{P}\}\,\|\zeta\|^2 \le V(e_1, e_2). \tag{23}$$

From (22), and given $1 < p < 2$, we obtain:

$$\left[(e_1^{\mathrm{T}}e_1)^{\frac{p}{3p-2}}\right]^{\frac{1-p}{p}} \ge \left(\frac{V(e_1, e_2)}{\lambda_{\min}\{\mathcal{P}\}}\right)^{\frac{1-p}{p}} \Rightarrow (e_1^{\mathrm{T}}e_1)^{\frac{1-p}{3p-2}} \ge \left(\frac{V(e_1, e_2)}{\lambda_{\min}\{\mathcal{P}\}}\right)^{\frac{1-p}{p}}. \tag{24}$$

$V(e_1, e_2)$ is differentiable everywhere except the subspace $S = \{[e_1^{\mathrm{T}}, e_2^{\mathrm{T}}]^{\mathrm{T}} \in \mathbb{R}^{2n} | e_1 = 0\}$. From (11) and Property (P1), we obtain the time derivative of ζ as follows,

$$\begin{aligned}\dot{\zeta} &= \begin{bmatrix} \phi_1'(e_1)\dot{e}_1 \\ \dot{e}_2 \end{bmatrix} = \begin{bmatrix} \phi_1'(e_1)(-k_1\phi_1(e_1)+e_2) \\ -k_2\phi_1'(e_1)\phi_1(e_1) \end{bmatrix} \\ &= \mathcal{D}(e_1)\mathcal{A}\zeta,\end{aligned} \tag{25}$$

where,

$$\begin{aligned}&\mathcal{D}(e_1) = \mathrm{diag}[\phi_1'(e_1), \phi_1'(e_1)] \in \mathbb{R}^{2n\times 2n}, \\ &\lambda_{\min}\left\{\mathcal{D}(e_1)\right\} = \lambda_{\min}\left\{\phi_1'(e_1)\right\}.\end{aligned} \tag{26}$$

Given the expression of $\dot{\zeta}$ in (25), we obtain the time derivative of $V(e_1, e_2)$ as follows:

$$\begin{aligned}\dot{V} &= \dot{\zeta}^{\mathrm{T}}\mathcal{P}\zeta + \zeta^{\mathrm{T}}\mathcal{P}\dot{\zeta} \\ &= \zeta^{\mathrm{T}}((\mathcal{D}(e_1)\mathcal{A})^{\mathrm{T}}\mathcal{P} + \mathcal{P}\mathcal{D}(e_1)\mathcal{A})\zeta \\ &= -\zeta^{\mathrm{T}}\bar{\mathcal{Q}}(e_1)\zeta,\end{aligned} \tag{27}$$

where $\bar{\mathcal{Q}}(e_1)$ is given by:

$$\begin{aligned}&\bar{\mathcal{Q}}(e_1) = (\mathcal{D}(e_1)\mathcal{A})^{\mathrm{T}}\mathcal{P} + \mathcal{P}\mathcal{D}(e_1)\mathcal{A} = \begin{bmatrix} \bar{\mathcal{Q}}_{11}(e_1) & \bar{\mathcal{Q}}_{12}(e_1) \\ \bar{\mathcal{Q}}_{12}(e_1) & \bar{\mathcal{Q}}_{22}(e_1) \end{bmatrix}, \\ &\bar{\mathcal{Q}}_{11}(e_1) = 2(k_1p_{11} + k_2p_{12})\phi_1'(e_1), \\ &\bar{\mathcal{Q}}_{12}(e_1) = (k_1p_{12} + k_2p_{22} - p_{11})\phi_1'(e_1), \\ &\bar{\mathcal{Q}}_{22}(e_1) = -2p_{12}\phi_1'(e_1).\end{aligned} \tag{28}$$

From (28) and (18), we obtain $\bar{\mathcal{Q}} = \mathcal{Q}\mathcal{D}(e_1)$. Thereafter, as $\mathcal{Q}$ and $\mathcal{D}(e_1)$ defined by (18) and (26), respectively, are positive definite, we obtain the following inequality on their eigenvalues:

$$\lambda_{\min}\left\{\mathcal{Q}\mathcal{D}(e_1)\right\} \geq \lambda_{\min}\left\{\mathcal{Q}\right\}\lambda_{\min}\left\{\mathcal{D}(e_1)\right\} > 0. \tag{29}$$

After substituting (29) into (27) and applying (14) of Property 2, we obtain:

$$\begin{aligned}\dot{V} &= -\zeta^{\mathrm{T}}(\mathcal{Q}\mathcal{D}(e_1))\zeta \\ &\leq -\lambda_{\min}\left\{\mathcal{Q}\mathcal{D}(e_1)\right\}\zeta^{\mathrm{T}}\zeta \\ &\leq -\lambda_{\min}\left\{\mathcal{D}(e_1)\right\}\lambda_{\min}\left\{\mathcal{Q}\right\}\zeta^{\mathrm{T}}\zeta\end{aligned} \tag{30}$$

As $\lambda_{\min}\left\{\mathcal{D}(e_1)\right\} = \lambda_{\min}\left\{\phi_1'(e_1)\right\}$, substituting (16), (22) and (24) into (30), we obtain:

$$\begin{aligned}\dot{V} &\leq -\left[k_3 + (e_1^{\mathrm{T}}e_1)^{\frac{1-p}{3p-2}}\frac{p}{3p-2}\right]\lambda_{\min}\left\{\mathcal{Q}\right\}\zeta^{\mathrm{T}}\zeta \\ &\leq -\frac{\lambda_{\min}\left\{\mathcal{Q}\right\}}{\lambda_{\max}\left\{\mathcal{P}\right\}}\left[k_3 + \left(\frac{V}{\lambda_{\min}\left\{\mathcal{P}\right\}}\right)^{\frac{1-p}{p}}\frac{p}{3p-2}\right]V \\ &\leq -\gamma_1 V - \gamma_2 V^{\frac{1}{p}},\end{aligned} \tag{31}$$

where γ_1 and γ_2 are positive constants defined by:

$$\begin{aligned}&\gamma_1 = k_3\frac{\lambda_{\min}\left\{\mathcal{Q}\right\}}{\lambda_{\max}\left\{\mathcal{P}\right\}} = k_3\frac{\lambda_{\min}\left\{\mathcal{Q}^*\right\}}{\lambda_{\max}\left\{\mathcal{P}^*\right\}}; \\ &\gamma_2 = \frac{\lambda_{\min}\left\{\mathcal{Q}\right\}\lambda_{\min}\left\{\mathcal{P}\right\}^{\frac{p-1}{p}}}{\lambda_{\max}\left\{\mathcal{P}\right\}}\frac{p}{3p-2} = \frac{\lambda_{\min}\left\{\mathcal{Q}^*\right\}\lambda_{\min}\left\{\mathcal{P}^*\right\}^{\frac{p-1}{p}}}{\lambda_{\max}\left\{\mathcal{P}^*\right\}}\frac{p}{3p-2}.\end{aligned} \tag{32}$$

Therefore, based on the inequality (31), Lemma 1 and Lemma 2, we conclude that the origin of the error dynamics (11) is fast finite-time stable. □

The following corollary describes the robustness of the differentiator perturbed by $\Delta^D \in \mathbb{R}^n$ in the second-order dynamics of (11). In the ESO design described in Section 5, $\Delta^D \in \mathbb{R}^n$ is corresponding with the time-derivatives of disturbance forces and torques.

Corollary 1 *(Perturbation Robustness). Consider the proposed HC-FFTSD under perturbation input $\Delta^D \in \mathbb{R}^n$, which satisfies $\|\Delta^D\| \leq \overline{\Delta^D}$. The differentiator perturbed by Δ^D is given by:*

$$\begin{aligned}\dot{e}_1 &= -k_1\phi_1(e_1) + e_2, \\ \dot{e}_2 &= -k_2\phi_2(e_1) + \Delta^D.\end{aligned} \tag{33}$$

If γ_1 in (32) satisfies $\gamma_1 \geq \lambda_{\max}\left\{\mathcal{P}\right\}/\lambda_{\min}\left\{\mathcal{P}\right\}$, then (33) is practically finite-time stable (PFTS).

Proof. By applying the Lyapunov function V defined by (19) in Theorem 1, and the perturbed differentiator given by (33), we obtain the time derivative of this Lyapunov function as follows:

Fig. 1. The multi-rotor vehicle and coordinate frames.

$$\begin{aligned}\dot{V} &\leq -\gamma_1 V - \gamma_2 V^{\frac{1}{p}} + [0^{\mathrm{T}}, (\Delta^D)^{\mathrm{T}}]\mathcal{P}\zeta + \zeta^{\mathrm{T}}\mathcal{P}[0^{\mathrm{T}}, (\Delta^D)^{\mathrm{T}}]^{\mathrm{T}} \\ &\leq -\gamma_1 V - \gamma_2 V^{\frac{1}{p}} + 2\lambda_{\max}\{\mathcal{P}\}\overline{\Delta^D}\|\zeta\|.\end{aligned} \tag{34}$$

Now applying Cauchy-Schwarz inequality and (20) to the inequality (34), we obtain:

$$\begin{aligned}\dot{V} &\leq -\gamma_1 V - \gamma_2 V^{\frac{1}{p}} + \lambda_{\max}\{\mathcal{P}\}\,||\zeta||^2 + \lambda_{\max}\{\mathcal{P}\}\,\overline{\Delta^D}^2 \\ &\leq -\left(\gamma_1 - \frac{\lambda_{\max}\{\mathcal{P}\}}{\lambda_{\min}\{\mathcal{P}\}}\right)V - \gamma_2 V^{\frac{1}{p}} + \lambda_{\max}\{\mathcal{P}\}\,\overline{\Delta^D}^2.\end{aligned} \tag{35}$$

Therefore, by applying Lemma 3 to the inequality (35), we conclude that the differentiator (33), which is the differentiator (11) under disturbance Δ^D, is PFTS. □

4. Problem formulation

4.1. Coordinate frame definition

The configuration of the vehicle, modeled as a rigid body, is given by its position and orientation, which are together referred to as its pose. To define the pose of the vehicle, we fix a coordinate frame $\mathcal{B}$ to its body and another coordinate frame $\mathcal{E}$ that is fixed in space as the inertial coordinate frame. Define $\mathbf{e}_i$ as the unit vector along the ith coordinate axis for $i = 1, 2, 3$. Let $b \in \mathbb{R}^3$ denote the position vector of the origin of frame $\mathcal{B}$ with respect to frame $\mathcal{E}$. The rigid body attitude is represented by the rotation matrix $R \in \mathrm{SO}(3)$ from frame $\mathcal{B}$ to frame $\mathcal{E}$. The special orthogonal group of rigid body rotations, SO(3), is defined by Murray et al. [29]:

$$\mathrm{SO}(3) = \left\{ R \in \mathbb{R}^{3\times 3},\ R^{\mathrm{T}}R = RR^{\mathrm{T}} = I,\ \det(R) = 1 \right\}.$$

$\mathrm{SO}(3) \subset \mathbb{R}^{3\times 3}$ is a matrix Lie group under matrix multiplication. The Lie algebra (tangent space at identity) of SO(3) is denoted $\mathfrak{so}(3)$ and defined by:

$$\mathfrak{so}(3) = \left\{ S \in \mathbb{R}^{3\times 3} \mid S + S^{\mathrm{T}} = 0 \right\}, \text{i.e. } S = s^{\times} = \begin{bmatrix} 0 & -s_3 & s_2 \\ s_3 & 0 & -s_1 \\ -s_2 & s_1 & 0 \end{bmatrix}.$$

Here $(.)^{\times} : \mathbb{R}^3 \to \mathfrak{so}(3)$ denotes the bijective map from three-dimensional Euclidean space to $\mathfrak{so}(3)$. For a vector $s = [s_1\ s_2\ s_3]^{\mathrm{T}} \in \mathbb{R}^3$, the matrix $s^{\times}$ represents the vector cross product operator, that is $s \times r = s^{\times} r$, where $r \in \mathbb{R}^3$. The inverse of $(.)^{\times}$ is denoted $\mathrm{vex}(.) : \mathfrak{so}(3) \to \mathbb{R}^3$, such that $\mathrm{vex}(a^{\times}) = a$, for all $a^{\times} \in \mathfrak{so}(3)$.

The attitude kinematics on SO(3) is expressed as: $\dot{R} = R\Omega^{\times}$, where $\Omega \in \mathbb{R}^3$ is the angular velocity in body-fixed frame $\mathcal{B}$. The tangent bundle of SO(3) is denoted by TSO(3), containing the collection of all of the tangent spaces for all points on SO(3). In attitude kinematics, we express TSO(3) to be $\mathrm{TSO}(3) = \left\{ (R, \Omega^{\times}) | R \in \mathrm{SO}(3), \Omega^{\times} \in \mathfrak{so}(3) \right\}$.

We represent the pose (attitude and position) of the rigid body by $(b, R) \in \mathrm{SE}(3)$, where b denotes the inertial position vector. The pose of the vehicle can be represented in matrix form as follows:

$$\mathrm{g} = \begin{bmatrix} R & b \\ 0 & 1 \end{bmatrix} \in \mathrm{SE}(3) \tag{36}$$

where SE(3), the special Euclidean group, is the six-dimensional Lie group of rigid body motions. A diagram of coordinate systems on SE(3) is presented in Fig. 1.

Applying the compactly represented pose given by (36), the velocity kinematics of the vehicle is given by:

$$\begin{cases} \dot{b} = v = Rv, \\ \dot{R} = R\Omega^{\times}, \end{cases} \text{ or } \dot{\mathrm{g}} = \mathrm{g}\xi,\ \xi = \begin{bmatrix} \Omega^{\times} & v \\ 0 & 0 \end{bmatrix} \in \mathfrak{se}(3) \tag{37}$$

where $v, v \in \mathbb{R}^3$ denote the translational velocity in frames $\mathcal{E}$ and $\mathcal{B}$ respectively. Similar to the tangent space of SO(3), ξ in (37) is on the tangent space of SE(3). We denote the tangent bundle of SE(3) to be $\mathrm{TSE}(3) = \{(\mathrm{g}, \xi) | \mathrm{g} \in \mathrm{SE}(3), \xi \in \mathfrak{se}(3)\}$.

4.2. System dynamics

The overall dynamics of a multi-rotor vehicle with a body-fixed plane of rotors are given by:

$$\begin{cases} \dot{b} = v = Rv \\ m\dot{v} = mg\mathbf{e}_3 - fR\mathbf{e}_3 + \varphi_D \\ \dot{R} = R\Omega^{\times} \\ J\dot{\Omega} = J\Omega \times \Omega + \tau + \tau_D \end{cases} \tag{38}$$

where $\mathbf{e}_3 = [0 \quad 0 \quad 1]^{\mathrm{T}}$, $f \in \mathbb{R}$ is the scalar thrust force, and $\tau \in \mathbb{R}^3$ is the control torque created by the rotors, g denotes the acceleration due to gravity and $m \in \mathbb{R}^+$ and $J = J^{\mathrm{T}} \in \mathbb{R}^{3\times3}$ are the mass and inertia matrix of the UAV, respectively. The force and torque disturbances are denoted φ_D and τ_D respectively, which are mainly due to unsteady aerodynamics.

We denote the onboard measurements b^m, v^m, R^m, Ω^m regarding b, v, R, Ω defined by (37). With the presence of measurement uncertainties, the measurements are modeled as follows:

$$b^m = b + \Delta_b^N, v^m = v + \Delta_v^N, R^m = R\exp((\Delta_R^N)^{\times}), \Omega^m = \Omega + \Delta_{\Omega}^N, \tag{39}$$

where $\Delta_b^N, \Delta_v^N, \Delta_R^N, \Delta_{\Omega}^N \in \mathbb{R}^3$ are uncertainties in position, velocity, attitude, and angular velocity measurements, respectively.

4.3. Morse function on SO(3)

The following Lemma is used in the design of the ESO for rotational motion scheme for the vehicle.

Lemma 5. [6] *Consider the attitude kinematics*

$$\dot{R} = R\Omega^{\times},\ R \in \mathrm{SO}(3),\ \Omega \in \mathbb{R}^3. \tag{40}$$

Define $K = \mathrm{diag}([K_1, K_2, K_3])$, *where* $K_1 > K_2 > K_3 \geq 1$. *Define*

$$s_K(R) = \sum_{i=1}^{3} K_i(R^{\mathrm{T}}\mathbf{e}_i) \times \mathbf{e}_i, \tag{41}$$

such that $\frac{\mathrm{d}}{\mathrm{d}t}\langle K, I - R\rangle = \Omega^{\mathrm{T}} s_K(R)$. *Here* $\langle A, B\rangle = \mathrm{tr}(A^{\mathrm{T}}B)$, *which makes* $\langle K, I - R\rangle$ *a Morse function defined on* SO(3) *with a discrete set of non-degenerate critical points. Let* $\mathcal{S} \subset \mathrm{SO}(3)$ *be a closed subset containing the identity in its interior, defined by*

$$\mathcal{S} = \left\{ R \in \mathrm{SO}(3) \ :\ R_{ii} \geq 0 \text{ and } R_{ij}R_{ji} \leq 0, \forall i,\ j \in \{1,2,3\},\ i \neq j \right\}. \tag{42}$$

Then $\forall\, R \in \mathcal{S}$, *we have*

$$s_K(R)^{\mathrm{T}} s_K(R) \geq \langle K, I - R\rangle. \tag{43}$$

Remark 1 *(Almost global domain of attraction).* [34] We know that the subset of SO(3) where $s_K(R) = 0, R \in \mathrm{SO}(3)$, which is also the set of critical points for $\langle I - R, K\rangle$, is

$$C \triangleq \{I, \mathrm{diag}(1,-1,-1), \mathrm{diag}(-1,1,-1), \mathrm{diag}(-1,-1,1)\} \subset \mathrm{SO}(3). \tag{44}$$

In addition, the global minimum of this Morse function is $R = I$.

4.4. ESO estimates and errors

The ESO on TSE(3) is split into a translational ESO design on vector space $\mathbb{R}^3$ and a ESO for rotational motion design on TSO(3). $(\widehat{b}, \widehat{v}, \widehat{\varphi}_D) \in \mathbb{R}^3 \times \mathbb{R}^3 \times \mathbb{R}^3$ denotes the estimated position, translational velocity, and disturbance force, as the states of the translational ESO. The estimation errors for the translational ESO are defined as follows:

$$e_b = b^m - \widehat{b}, e_v = v^m - \widehat{v}, e_{\varphi} = \varphi_D - \widehat{\varphi}_D, \tag{45}$$

which are estimation errors of position, translational velocity, and total disturbance force respectively.

Let $(\widehat{R}, \widehat{\Omega}, \widehat{\tau}_D) \in \mathrm{SO}(3) \times \mathbb{R}^3 \times \mathbb{R}^3$ denote the estimated attitude, angular velocity, and disturbance torque states provided by the ESO for rotational motion. For the ESO for rotational motion, the error states are defined as follows. The attitude estimation error is defined by:

$$E_R = \widehat{R}^{\mathrm{T}} R^m, \tag{46}$$

on the group of rigid body rotations, SO(3), which is not a vector space. The angular velocity estimation error, e_{Ω}, and torque disturbance estimation error, e_{τ}, are expressed on the vector space $\mathbb{R}^3$, and are defined as:

$$e_{\Omega} = \Omega^m - E_R^{\mathrm{T}}\widehat{\Omega},\ e_{\tau} = \tau_D - \widehat{\tau}_D. \tag{47}$$

A properly designed ESO on TSE(3) can stabilize the error states at $(e_b, e_v, e_{\varphi}, E_R, e_{\Omega}, e_{\tau}) = (0,0,0,I,0,0)$ when there are no measurement uncertainties and dynamic disturbances, such that $\Delta_b^N, \Delta_v^N, \Delta_R^N, \Delta_{\Omega}^N = 0$, and $\dot{\varphi}_D, \dot{\tau}_D = 0$. Moreover, when the measurement uncertainties and dynamic

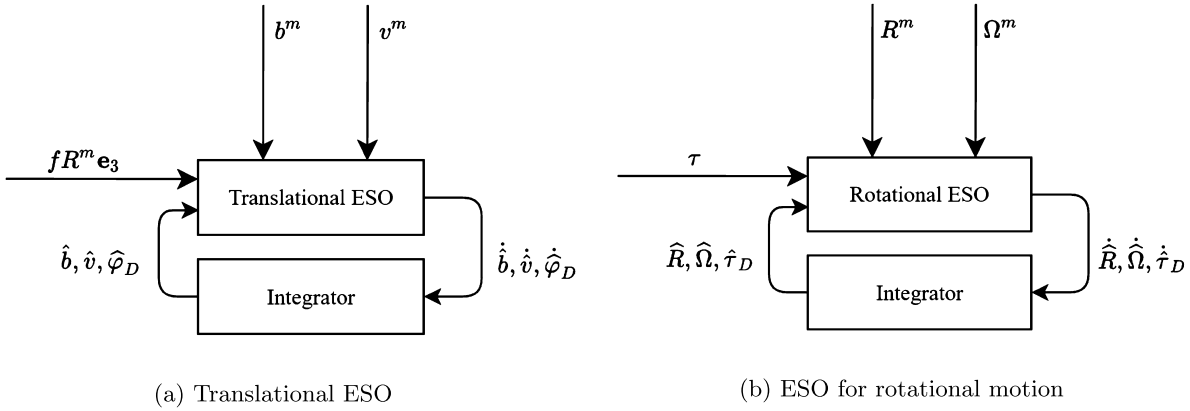

(a) Translational ESO (b) ESO for rotational motion

Fig. 2. Block diagrams of the proposed ESO.

disturbances are non-negligible, we expect the ESO to drive the error states to a small neighborhood around $(0,0,0,I,0,0)$. The input-output relationship of the ESO is presented in Fig. 2.

5. Fast finite-time stable extended state observer (FFTS-ESO) on TSE(3)

In this section, we present the FFTS-ESO on TSE(3). As mentioned in the previous section, the ESO design on TSE(3) is given by an ESO for the translational motion on the vector space $\mathbb{R}^3$ to estimate the resultant disturbance force, and an ESO for rotational motion on TSO(3) to estimate the resultant disturbance torque. We present the two ESO designs along with their stability and robustness results.

5.1. ESO for translational motion

Proposition 1 *(Translational ESO on $\mathbb{R}^3$). Define constant positive scalar gains k_{t1} and k_{t2}, which make the matrix $\mathcal{A}_t \in \mathbb{R}^{2\times 2}$ defined as:*

$$\mathcal{A}_t = \begin{bmatrix} -k_{t1} & 1 \\ -k_{t2} & 0 \end{bmatrix}, \tag{48}$$

a Hurwitz matrix. In addition, define the constant k_{t3} that replaces k_3 in the functions $\phi_1(\cdot)$ and $\phi_2(\cdot)$ defined by (9). Then the ESO designed for the translational motion is given by:

$$\begin{aligned} \dot{\hat{b}} &= \hat{v}, \\ m\dot{\hat{v}} &= mg\mathbf{e}_3 - fR^m\mathbf{e}_3 + mk_{t1}\phi_1(\psi_t) + m\kappa_t\left[(e_b^{\mathrm{T}}e_b)^{\frac{1-p}{p}} H\left(e_b, \frac{p-1}{p}\right)e_v + e_v\right] + \hat{\varphi}_D, \\ \dot{\hat{\varphi}}_D &= mk_{t2}\phi_2(\psi_t), \end{aligned} \tag{49}$$

where ψ_t is defined as:

$$\psi_t = e_v + \kappa_t\left[e_b + (e_b^{\mathrm{T}}e_b)^{\frac{1-p}{p}} e_b\right],\ \kappa_t > 1/2. \tag{50}$$

Theorem 2. *Given the observer errors for the translational ESO defined by (45), the translational kinematics and dynamics given by (38), and the ESO for translational motion given by Proposition 1, the error dynamics of this translational ESO is given by:*

$$\begin{aligned} \dot{e}_b &= e_v, \\ m\dot{e}_v &= -mk_{t1}\phi_1(\psi_t) - m\kappa_t\left[(e_b^{\mathrm{T}}e_b)^{\frac{1-p}{p}} H\left(e_b, \frac{p-1}{p}\right)e_v + e_v\right] + e_\varphi, \\ \dot{e}_\varphi &= -mk_{t2}\phi_2(\psi_t) + \dot{\varphi}_D. \end{aligned} \tag{51}$$

The error dynamics (51) is FFTS at the origin $((e_b, e_v, e_\varphi) = (0,0,0))$ when the resultant disturbance force is constant $(\dot{\varphi}_D = 0)$.

Proof. Simplify (51) as follows:

$$\begin{aligned} \dot{\psi}_t &= -k_{t1}\phi_1(\psi_t) + m^{-1}e_\varphi, \\ m^{-1}\dot{e}_\varphi &= -k_{t2}\phi_2(\psi_t) + m^{-1}\dot{\varphi}_D. \end{aligned} \tag{52}$$

Next, for $\mathcal{A}_t$ as defined in (48), $\forall\, \mathcal{Q}_t \in \mathbb{R}^{2\times 2}$ where $\mathcal{Q}_t \succ 0$, the Lyapunov equation,

$$\mathcal{A}_t^{\mathrm{T}}\mathcal{P}_t + \mathcal{P}_t\mathcal{A}_t = -\mathcal{Q}_t, \tag{53}$$

has a unique solution $\mathcal{P}_t$. Thereafter, define the Lyapunov function:

$$V_t = V_{t0} + \mu_t e_b^{\mathrm{T}}e_b, \text{ where } V_{t0} = \zeta_t^{\mathrm{T}}\mathcal{P}_t\zeta_t \tag{54}$$

and ζ_t is defined as follows:

$$\zeta_t = [\phi_1^{\mathrm{T}}(\psi_t),\ m^{-1}e_\varphi^{\mathrm{T}}]^{\mathrm{T}}.$$

We constrain the positive scalar μ_t in (54) as:

$$0 < \mu_t < k_{t3}^3 \frac{\lambda_{\min}\{\mathcal{P}_t\}\,\lambda_{\min}\{\mathcal{Q}_t\}}{\lambda_{\max}\{\mathcal{P}_t\}}. \tag{55}$$

From Theorem 1, (52) and (23), we find that the time-derivative of V_t satisfies:

$$\dot{V}_t \le -\gamma_{t1}V_{t0} - \gamma_{t2}V_{t0}^{\frac{1}{p}} + 2\mu_t e_b^{\mathrm{T}} e_v, \tag{56}$$

where γ_{t1} and γ_{t2} are defined by:

$$\gamma_{t1} = k_{t3}\frac{\lambda_{\min}\{\mathcal{Q}_t\}}{\lambda_{\max}\{\mathcal{P}_t\}},\ \gamma_{t2} = \frac{\lambda_{\min}\{\mathcal{Q}_t\}\,\lambda_{\min}\{\mathcal{P}_t\}^{\frac{p-1}{p}}\,p}{\lambda_{\max}\{\mathcal{P}_t\}\,(3p-2)}. \tag{57}$$

Substituting (50) into (56), we obtain:

$$\begin{aligned}
\dot{V}_t &\le -\gamma_{t1}V_{t0} - \gamma_{t2}V_{t0}^{\frac{1}{p}} + 2\mu_t e_b^{\mathrm{T}}\left[\psi_t - \kappa_t e_b - \kappa_t (e_b^{\mathrm{T}}e_b)^{\frac{1-p}{p}} e_b\right] \\
&\le -\gamma_{t1}V_{t0} - \gamma_{t2}V_{t0}^{\frac{1}{p}} + 2\mu_t e_b^{\mathrm{T}}\psi_t - 2\mu_t\kappa_t e_b^{\mathrm{T}}e_b - 2\mu_t\kappa_t (e_b^{\mathrm{T}}e_b)^{\frac{1}{p}} \\
&\le -\gamma_{t1}V_{t0} - \gamma_{t2}V_{t0}^{\frac{1}{p}} - 2\mu_t\kappa_t e_b^{\mathrm{T}}e_b - 2\mu_t\kappa_t (e_b^{\mathrm{T}}e_b)^{\frac{1}{p}} + \mu_t\psi_t^{\mathrm{T}}\psi_t + \mu_t e_b^{\mathrm{T}}e_b \\
&\le -\left(\gamma_{t1} - \frac{\mu_t}{k_{t3}^2\lambda_{\min}\{\mathcal{P}_t\}}\right)V_{t0} - \gamma_{t2}V_{t0}^{\frac{1}{p}} - (2\kappa_t - 1)\mu_t e_b^{\mathrm{T}}e_b - 2\kappa_t\mu_t^{\frac{p-1}{p}}\mu_t^{\frac{1}{p}}(e_b^{\mathrm{T}}e_b)^{\frac{1}{p}}.
\end{aligned} \tag{58}$$

Therefore, we further obtain:

$$\dot{V}_t < -\Gamma_{t1}V_t - \Gamma_{t2}V_t^{\frac{1}{p}}, \tag{59}$$

where

$$\begin{aligned}
\Gamma_{t1} &= \min\left\{k_{t3}\frac{\lambda_{\min}\{\mathcal{Q}_t\}}{\lambda_{\max}\{\mathcal{P}_t\}} - \frac{\mu_t}{k_{t3}^2\lambda_{\min}\{\mathcal{P}_t\}}, 2\kappa_t - 1\right\}, \\
\Gamma_{t2} &= \min\left\{\frac{\lambda_{\min}\{\mathcal{Q}_t\}\,\lambda_{\min}\{\mathcal{P}_t\}^{\frac{p-1}{p}}\,p}{\lambda_{\max}\{\mathcal{P}_t\}\,(3p-2)}, 2\kappa_t\mu_t^{\frac{p-1}{p}}\right\}.
\end{aligned} \tag{60}$$

Based on (59), we conclude that when the resultant disturbance force is constant ($\dot{\varphi}_D = 0$) and the ESO gains are constrained according to Proposition 1, the error dynamics of ESO (51) is FFTS. This concludes the proof of Theorem 2. □

By applying the stability proof of HC-FFTSD presented in Theorem 1, Theorem 2 shows that the proposed ESO in translational dimension is fast finite-time stable when the disturbance force is a constant. Now, we apply Corollary 1 to investigate robustness of the proposed ESO against dynamic disturbance force.

Corollary 2. *Consider the error dynamics of translational ESO given by (51) when the resultant disturbance force is dynamic ($\dot{\varphi}_D \neq 0$). If γ_{t1} defined by (57) satisfies:*

$$\gamma_{t1} \ge \frac{\lambda_{\max}\{\mathcal{P}_t\}}{m\lambda_{\min}\{\mathcal{P}_t\}}$$

and the magnitude of the time derivative of the disturbance force is upper bounded according to $\|\dot{\varphi}_D\| \le \overline{\Delta\varphi}$, this error dynamics is PFTS.

Proof. We apply the Lyapunov function defined by (54), but constrain the positive scalar μ_t as:

$$0 < \mu_t < k_{t3}^2\lambda_{\min}\{\mathcal{P}_t\}\left(k_{t3}\frac{\lambda_{\min}\{\mathcal{Q}_t\}}{\lambda_{\max}\{\mathcal{P}_t\}} - \frac{\lambda_{\max}\{\mathcal{P}_t\}}{m\lambda_{\min}\{\mathcal{P}_t\}}\right). \tag{61}$$

Thereafter, from Theorem 1, Corollary 1, (51) and (23), we find that the time-derivative of V_t satisfies:

$$\begin{aligned}
\dot{V}_t &\le -\gamma_{t1}V_{t0} - \gamma_{t2}V_{t0}^{\frac{1}{p}} + 2\mu_t e_b^{\mathrm{T}}e_v + [0^{\mathrm{T}}, (m^{-1}\dot{\varphi}_D)^{\mathrm{T}}]\mathcal{P}_t\zeta_t + \zeta_t^{\mathrm{T}}\mathcal{P}_t[0^{\mathrm{T}}, (m^{-1}\dot{\varphi}_D)^{\mathrm{T}}]^{\mathrm{T}}, \\
&\le -\gamma_{t1}V_{t0} - \gamma_{t2}V_{t0}^{\frac{1}{p}} + 2\mu_t e_b^{\mathrm{T}}e_v + 2m^{-1}\lambda_{\max}\{\mathcal{P}_t\}\,\overline{\Delta\varphi}\|\zeta_t\|,
\end{aligned} \tag{62}$$

where γ_{t1}, γ_{t2} are defined by (57). By applying Cauchy-Schwartz inequality to (62), we obtain:

$$\dot{V}_t \leq -\left(k_{t3}\frac{\lambda_{\min}\{\mathcal{Q}_t\}}{\lambda_{\max}\{\mathcal{P}_t\}} - \frac{\lambda_{\max}\{\mathcal{P}_t\}}{m\lambda_{\min}\{\mathcal{P}_t\}}\right)V_t - \gamma_{t2}V_t^{\frac{1}{p}} + 2\mu_t e_b^{\mathrm{T}} e_v + \frac{\lambda_{\max}\{\mathcal{P}_t\}\overline{\Delta^{\varphi}}^2}{m}. \tag{63}$$

By applying the derivation similar to (58), we obtain

$$\begin{aligned}\dot{V}_t \leq &-\left(k_{t3}\frac{\lambda_{\min}\{\mathcal{Q}_t\}}{\lambda_{\max}\{\mathcal{P}_t\}} - \frac{\lambda_{\max}\{\mathcal{P}_t\}}{m\lambda_{\min}\{\mathcal{P}_t\}} - \frac{\mu_t}{k_{t3}^2\lambda_{\min}\{\mathcal{P}_t\}}\right)V_t - \gamma_{t2}V_t^{\frac{1}{p}} \\ &- (2\kappa_t - 1)\mu_t e_b^{\mathrm{T}} e_b - 2\kappa_t \mu_t^{\frac{p-1}{p}}\mu_t^{\frac{1}{p}}(e_b^{\mathrm{T}} e_b)^{\frac{1}{p}} + \frac{\lambda_{\max}\{\mathcal{P}_t\}\overline{\Delta^{\varphi}}^2}{m}.\end{aligned} \tag{64}$$

Considering that μ_t is constrained by (61), we further obtain:

$$\dot{V}_t < -\Gamma_{t1}^* V_t - \Gamma_{t2}^* V_t^{\frac{1}{p}} + \frac{\lambda_{\max}\{\mathcal{P}_t\}\overline{\Delta^{\varphi}}^2}{m}. \tag{65}$$

We omit the expression of positive scalars Γ_{t1}^* and Γ_{t2}^* for brevity. Based on (65), we conclude that when the time derivative of disturbance force φ_D, $\dot{\varphi}_D$, is upper bounded, and the ESO gains are constrained according to Corollary 2, the error dynamics of ESO (51) is PFTS. This concludes the proof of Corollary 2. □

5.2. ESO for rotational motion

Proposition 2 *(ESO for rotational motion). Define $e_R = s_K(E_R)$, where $s_K(\cdot)$ is as defined by Lemma 5. Define $e_w(E_R, e_\Omega)$ as follows:*

$$e_w(E_R, e_\Omega) = \frac{\mathrm{d}}{\mathrm{d}t}e_R = \sum_{i=1}^{3} K_i \mathbf{e}_i \times (e_\Omega \times E_R^{\mathrm{T}}\mathbf{e}_i). \tag{66}$$

Define constant positive scalar gains k_{a1} and k_{a2}, which make the matrix $\mathcal{A}_a \in \mathbb{R}^{2\times 2}$ defined by:

$$\mathcal{A}_a = \begin{bmatrix} -k_{a1} & 1 \\ -k_{a2} & 0 \end{bmatrix}, \tag{67}$$

a Hurwitz matrix. In addition, define the constant k_{a3} to replace k_3 in the functions $\phi_1(\cdot)$ and $\phi_2(\cdot)$ defined by (9). Then the ESO designed for the rotational motion is given by:

$$\begin{aligned}&\dot{\hat{R}} = \hat{R}\hat{\Omega}^{\times}, \\ &\dot{\hat{\Omega}} = E_R J^{-1}\left[J\Omega^m \times \Omega^m + \hat{\tau}_D + \tau + k_{a1}J\phi_1(\psi_a) + \kappa_a J(e_R^{\mathrm{T}}e_R)^{\frac{1-p}{p}} H\left(e_R, \frac{p-1}{p}\right)e_w\right] \\ &+ E_R J^{-1}(\kappa_a J e_w) + E_R e_\Omega^{\times} E_R^{\mathrm{T}}\hat{\Omega}, \\ &\dot{\hat{\tau}}_D = J k_{a2}\phi_2(\psi_a),\end{aligned} \tag{68}$$

where ψ_a is defined as:

$$\psi_a = e_\Omega + \kappa_a\left[e_R + (e_R^{\mathrm{T}}e_R)^{\frac{1-p}{p}} e_R\right],\ \kappa_a > \frac{1}{2}. \tag{69}$$

Theorem 3. *Given the observer errors for the ESO for rotational motion defined by (47), the rotational kinematics and dynamics given by (38), and the ESO for rotational motion given in Proposition 2, the error dynamics of this ESO is given by:*

$$\begin{aligned}&\dot{E}_R = E_R e_\Omega^{\times}, \\ &J\dot{e}_\Omega = -k_{a1}J\phi_1(\psi_a) - \kappa_a J\left[(e_R^{\mathrm{T}}e_R)^{\frac{1-p}{p}} H\left(e_R, \frac{p-1}{p}\right)e_w + e_w\right] + e_\tau, \\ &\dot{e}_\tau = -k_{a2}J\phi_2(\psi_a) + \dot{\tau}_D.\end{aligned} \tag{70}$$

The error dynamics (70) is almost globally FFTS at the origin ($(E_R, e_\Omega, e_\tau) = (I, 0, 0)$) when the resultant disturbance torque is constant ($\dot{\tau}_D = 0$).

Proof. Simplify (70) as follows:

$$\begin{aligned}\dot{\psi}_a &= -k_{a1}\phi_1(\psi_a) + J^{-1}e_\tau, \\ J^{-1}\dot{e}_\tau &= -k_{a2}\phi_2(\psi_a) + J^{-1}\dot{\tau}_D.\end{aligned} \tag{71}$$

Next, for $\mathcal{A}_a$ as defined in (67), $\forall\, \mathcal{Q}_a \in \mathbb{R}^{2\times 2}$ where $\mathcal{Q}_a \succ 0$, the Lyapunov equation:

$$\mathcal{A}_a^{\mathrm{T}}\mathcal{P}_a + \mathcal{P}_a\mathcal{A}_a = -\mathcal{Q}_a, \tag{72}$$

has a unique solution $\mathcal{P}_a$. Thereafter, define the Morse-Lyapunov function:

$$V_a = V_{a0} + \mu_a\langle K, I - E_R\rangle,\ \text{where } V_{a0} = \zeta_a^{\mathrm{T}}\mathcal{P}_a\zeta_a, \tag{73}$$

μ_a is a positive scalar, and ζ_a is defined as:

$$\zeta_a = [\phi_1^{\mathrm{T}}(\psi_a),\ J^{-1}e_\tau^{\mathrm{T}}]^{\mathrm{T}}.$$

We constrain the positive scalar μ_a in (73) as follows:

$$0 < \mu_a < 2k_{a3}^3 \frac{\lambda_{\min}\{\mathcal{P}_a\}\,\lambda_{\min}\{\mathcal{Q}_a\}}{\lambda_{\max}\{\mathcal{P}_a\}}. \tag{74}$$

From Theorem 1, (71) and (23), we find that the time-derivative of V_a satisfies:

$$\dot{V}_a \le -\gamma_{a1}V_{a0} - \gamma_{a2}V_{a0}^{\frac{1}{p}} + \mu_a e_R^{\mathrm{T}} e_\Omega, \tag{75}$$

where γ_{a1} and γ_{a2} are defined by:

$$\gamma_{a1} = k_{a3}\frac{\lambda_{\min}\{\mathcal{Q}_a\}}{\lambda_{\max}\{\mathcal{P}_a\}},\ \gamma_{a2} = \frac{\lambda_{\min}\{\mathcal{Q}_a\}\,\lambda_{\min}\{\mathcal{P}_a\}^{\frac{p-1}{p}}\,p}{\lambda_{\max}\{\mathcal{P}_a\}\,(3p-2)}. \tag{76}$$

Substituting (69) into (75), we obtain:

$$\begin{aligned}
\dot{V}_a &\le -\gamma_{a1}V_{a0} - \gamma_{a2}V_{a0}^{\frac{1}{p}} + \mu_a e_R^{\mathrm{T}}\left[\psi_a - \kappa_a e_R - \kappa_a (e_R^{\mathrm{T}}e_R)^{\frac{1-p}{p}} e_R\right] \\
&\le -\gamma_{a1}V_{a0} - \gamma_{a2}V_{a0}^{\frac{1}{p}} + \frac{1}{2}\mu_a\left(e_R^{\mathrm{T}}e_R + \psi_a^{\mathrm{T}}\psi_a\right) - \kappa_a\mu_a\left[e_R^{\mathrm{T}}e_R + (e_R^{\mathrm{T}}e_R)^{\frac{1}{p}}\right] \\
&\le -\left(\gamma_{a1} - \frac{\mu_a}{2k_{a3}^2\lambda_{\min}\{\mathcal{P}_a\}}\right)V_{a0} - \gamma_{a2}V_{a0}^{\frac{1}{p}} - \left(\kappa_a - \frac{1}{2}\right)\mu_a e_R^{\mathrm{T}}e_R - \kappa_a\mu_a(e_R^{\mathrm{T}}e_R)^{\frac{1}{p}}.
\end{aligned} \tag{77}$$

By applying Lemma 5 on (75), we obtain:

$$\begin{aligned}
\dot{V}_a \le &-\left(\gamma_{a1} - \frac{\mu_a}{2k_{a3}^2\lambda_{\min}\{\mathcal{P}_a\}}\right)V_{a0} - \gamma_{a2}V_{a0}^{\frac{1}{p}} \\
&- \left(\kappa_a - \frac{1}{2}\right)\mu_a\langle K, I - E_R\rangle - \kappa_a\mu_a^{\frac{p-1}{p}}\mu_a^{\frac{1}{p}}\langle K, I - E_R\rangle^{\frac{1}{p}}.
\end{aligned} \tag{78}$$

After some algebra, we further obtain:

$$\dot{V}_a \le -\Gamma_{a1}V_a - \Gamma_{a2}V_a^{\frac{1}{p}}, \tag{79}$$

where:

$$\begin{aligned}
\Gamma_{a1} &= \min\left\{k_{a3}\frac{\lambda_{\min}\{\mathcal{Q}_a\}}{\lambda_{\max}\{\mathcal{P}_a\}} - \frac{\mu_a}{2k_{a3}^2\lambda_{\min}\{\mathcal{P}_a\}}, \kappa_a - \frac{1}{2}\right\}, \\
\Gamma_{a2} &= \min\left\{\frac{\lambda_{\min}\{\mathcal{Q}_a\}\,\lambda_{\min}\{\mathcal{P}_a\}^{\frac{p-1}{p}}\,p}{\lambda_{\max}\{\mathcal{P}_a\}\,(3p-2)}, \kappa_a\mu_a^{\frac{p-1}{p}}\right\}.
\end{aligned} \tag{80}$$

Considering the expression given by (79), the set where $\dot{V}_a = 0$ is:

$$\begin{aligned}
\dot{V}_a^{-1}(0) &= \left\{(E_R, e_\Omega, e_\tau) : s_K(E_R) = 0, \text{and } \zeta_a = 0\right\} \\
&= \left\{(E_R, e_\Omega, e_\tau) : E_R \in C, e_\Omega = 0, \text{and } e_\tau = 0\right\},
\end{aligned} \tag{81}$$

where C is as defined by (44), which gives the set of the critical points of the Morse function used as part of the Morse-Lyapunov function in (73). Using Theorem 8.4 from [19], we conclude that (E_R, e_Ω, e_τ) converge to the set:

$$S = \left\{(E_R, e_\Omega, e_\tau) \in \mathrm{SO}(3)\times\mathbb{R}^3\times\mathbb{R}^3 : E_R \in C, e_\Omega = 0, \text{and } e_\tau = 0\right\}, \tag{82}$$

in finite time. Based on (79), and Lemma 2, we conclude that when the observer gains satisfy the constraints in Proposition 2, the error dynamics (70) converges to the set S in finite time.

In S, the only stable equilibrium is $(I, 0, 0)$, while the other three are unstable. The resulting closed-loop system with the estimation errors gives rise to a Hölder-continuous feedback with exponent less than one ($1/2 < 1/p < 1$), while in the limiting case of $p = 1$, the feedback system is Lipschitz-continuous. Proceeding with a topological equivalence-based analysis similar to the one by Bohn and Sanyal [6], we conclude that the equilibrium and the corresponding regions of attraction of the ESO for rotational motion with $p \in]1, 2[$, are identical to those of the corresponding Lipschitz-continuous asymptotically stable ESO with $p = 1$, and the region of attraction is almost global.

To summarize, we conclude that the error dynamics (70) is almost globally FFTS (AG-FFTS) at the origin ($(E_R, e_\Omega, e_\tau) = (I, 0, 0)$) when the resultant disturbance torque is constant ($\dot{\tau}_D = 0$) and the observer gains are constrained according to Proposition 2. This concludes the proof of Theorem 3. □

We now present robustness of the proposed ESO against dynamic disturbance torque.

Corollary 3. *Consider the error dynamics of the rotational ESO given by (70) when the resultant disturbance torque is dynamic ($\dot{\tau}_D \neq 0$). If γ_{a1} defined by (76) satisfies:*

$$\gamma_{a1} \geq \frac{\lambda_{\max}\{\mathcal{P}_a\}}{\lambda_{\min}\{\mathcal{P}_a\}}$$

and the magnitude of the time derivative of disturbance torque is upper bounded according to $\|\dot{\tau}_D\| \leq \overline{\Delta^\tau}$, this error dynamics is PFTS.

Proof. We apply the Morse-Lyapunov function defined by (73), but constrain the positive scalar μ_a as:

$$0 < \mu_a < 2k_{a3}^2 \lambda_{\min}\{\mathcal{P}_a\} \left(k_{a3} \frac{\lambda_{\min}\{\mathcal{Q}_a\}}{\lambda_{\max}\{\mathcal{P}_a\}} - \frac{\lambda_{\max}\{\mathcal{P}_a\}}{\lambda_{\min}\{\mathcal{P}_a\}} \right). \tag{83}$$

Thereafter, from Theorem 1, Corollary 1, (70) and (23), we find that the time-derivative of V_t satisfies:

$$\begin{aligned} \dot{V}_a &\leq -\gamma_{a1} V_{a0} - \gamma_{a2} V_{a0}^{\frac{1}{p}} + \mu_a e_R^{\mathrm{T}} e_\Omega + [0^{\mathrm{T}}, (J^{-1}\dot{\tau}_D)^{\mathrm{T}}] \mathcal{P}_a \zeta_a + \zeta_a^{\mathrm{T}} \mathcal{P}_a [0^{\mathrm{T}}, (J^{-1}\dot{\tau}_D)^{\mathrm{T}}]^{\mathrm{T}}, \\ &\leq -\gamma_{a1} V_{a0} - \gamma_{a2} V_{a0}^{\frac{1}{p}} + \mu_a e_R^{\mathrm{T}} e_\Omega + 2\lambda_{\min}\{J\}^{-1} \lambda_{\max}\{\mathcal{P}_a\} \overline{\Delta^\tau} \|\zeta_a\|, \end{aligned} \tag{84}$$

where γ_{a1}, γ_{a2} are defined by (76). By applying Cauchy-Schwartz inequality to (84), we obtain:

$$\dot{V}_a \leq -\left(k_{a3} \frac{\lambda_{\min}\{\mathcal{Q}_a\}}{\lambda_{\max}\{\mathcal{P}_a\}} - \frac{\lambda_{\max}\{\mathcal{P}_a\}}{\lambda_{\min}\{\mathcal{P}_a\}} \right) V_a - \gamma_{a2} V_a^{\frac{1}{p}} + \mu_a e_R^{\mathrm{T}} e_\Omega + \frac{\lambda_{\max}\{\mathcal{P}_a\} \overline{\Delta^\tau}^2}{\lambda_{\min}\{J\}^2}. \tag{85}$$

By applying the derivation similar to (77), we obtain

$$\begin{aligned} \dot{V}_a &\leq -\left(k_{a3} \frac{\lambda_{\min}\{\mathcal{Q}_a\}}{\lambda_{\max}\{\mathcal{P}_a\}} - \frac{\lambda_{\max}\{\mathcal{P}_a\}}{\lambda_{\min}\{\mathcal{P}_a\}} - \frac{\mu_a}{2k_{a3}^2 \lambda_{\min}\{\mathcal{P}_a\}} \right) V_a - \gamma_{a2} V_a^{\frac{1}{p}} \\ &\quad - \left(\kappa_a - \frac{1}{2} \right) \mu_a e_R^{\mathrm{T}} e_R - 2\kappa_a \mu_a^{\frac{p-1}{p}} \mu_a^{\frac{1}{p}} (e_R^{\mathrm{T}} e_R)^{\frac{1}{p}} + \frac{\lambda_{\max}\{\mathcal{P}_a\} \overline{\Delta^\tau}^2}{\lambda_{\min}\{J\}^2} \\ &\leq -\left(k_{a3} \frac{\lambda_{\min}\{\mathcal{Q}_a\}}{\lambda_{\max}\{\mathcal{P}_a\}} - \frac{\lambda_{\max}\{\mathcal{P}_a\}}{\lambda_{\min}\{\mathcal{P}_a\}} - \frac{\mu_a}{2k_{a3}^2 \lambda_{\min}\{\mathcal{P}_a\}} \right) V_{a0} - \gamma_{a2} V_{a0}^{\frac{1}{p}} \\ &\quad - \left(\kappa_a - \frac{1}{2} \right) \mu_a \langle K, I - E_R \rangle - \kappa_a \mu_a^{\frac{p-1}{p}} \mu_a^{\frac{1}{p}} \langle K, I - E_R \rangle^{\frac{1}{p}} + \frac{\lambda_{\max}\{\mathcal{P}_a\} \overline{\Delta^\tau}^2}{\lambda_{\min}\{J\}^2}. \end{aligned} \tag{86}$$

Considering that μ_a is constrained by (83), we further obtain:

$$\dot{V}_a < -\Gamma_{a1}^* V_t - \Gamma_{a2}^* V_a^{\frac{1}{p}} + \frac{\lambda_{\max}\{\mathcal{P}_a\} \overline{\Delta^\tau}^2}{\lambda_{\min}\{J\}^2}. \tag{87}$$

We omit the expression of positive scalars Γ_{a1}^* and Γ_{a2}^* for brevity. Based on (87), we conclude that when the time derivative of disturbance torque τ_D, $\dot{\tau}_D$, is upper bounded, and the ESO gains are constrained according to Corollary 3, the error dynamics of ESO (70) is PFTS. This concludes the proof of Corollary 3. □

Remark 2 *(Comparative analysis of noise robustness: FFTS-ESO vs FxTSDO by Liu et al. [22]).* We investigate the disturbance (force and torque) observers given by theorems 1 and 2 in [22], abbreviated here as FxTSDO. The input of FxTSDO relies on the motion signals, X_2, Y_2, which represent translational and angular velocities, and $\dot{X}_2$, $\dot{Y}_2$, which represent translational and angular accelerations, respectively. However, the high-level noise associated with the translational acceleration obtained from an accelerometer restricts its direct use in a flight control scheme. Additionally, direct measurement of angular acceleration is usually not feasible. Furthermore, if $\dot{X}_2$ and $\dot{Y}_2$ are obtained from finite differencing of X_2 and Y_2, they will have higher noise levels than X_2 and Y_2, leading to inferior disturbance estimation performance. In contrast to FxTSDO, the proposed FFTS-ESO incorporates measured position and attitude signals, which have lower noise levels. Consequently, FFTS-ESO outperforms FxTSDO in terms of disturbance estimation performance, despite the theoretical fixed-time stability of FxTSDO. We show this through our numerical simulations in Section 6.

6. Numerical simulations

In this section, we compare the proposed FFTS-ESO with existing disturbance estimation schemes, which are LESO by Shao et al. [36] and FxTSDO by Liu et al. [22], on their disturbance estimation performance in four different simulated flight trajectories b^d, with and without the presence of measurement noises. The inertia and mass of the simulated multi-rotor vehicle are $J = \mathrm{diag}([0.0820, 0.0845, 0.1377])\,\mathrm{kg}\cdot\mathrm{m}^2$, $m = 4.34\,\mathrm{kg}$ by Pounds et al. [31]. Since the goal of the simulation is to validate and compare the disturbance estimation performance, the actuator dynamics and saturation are not included in the results reported in this section. The tracking control scheme to drive the vehicle to track the desired trajectories is developed based on the control scheme reported by Viswanathan et al. [40,39]. As this scheme is not a contribution of this article, we omit its description for brevity. We use MATLAB/Simulink with its ODE2 (Heun method) solver to conduct this set of simulations. The time step size is $h = 0.001\,\mathrm{s}$ and the simulated duration is $T = 30\,\mathrm{s}$.

Table 1
Flight trajectories to be tracked for the comparisons between LESO, FxTSDO, and FFTS-ESO.

Hovering (HV)	$b^d(t) = [0,\ 0,\ -3]^{\mathrm{T}}$ m
Slow swing (SS)	$b^d(t) = [10\sin(0.1\pi t),\ 0,\ -3]^{\mathrm{T}}$ m
Fast swing (FS)	$b^d(t) = [5\sin(0.5\pi t),\ 0,\ -3]^{\mathrm{T}}$ m
High pitch (HP)	$b^d(t) = [10\sin(0.5\pi t),\ 10\cos(0.5\pi t),\ -3]^{\mathrm{T}}$ m

Table 2
Measurement noise level in power spectral density for the comparisons between LESO, FxTSDO, and FFTS-ESO.

b^m	$b^m = b + \Delta_b^N$	$\Delta_b^N \sim P_b = 3e^{-8}$
v^m	$v^m = v + \Delta_v^N$	$\Delta_v^N \sim P_v = 3e^{-7}$
R^m	$R^m = R\exp(\Delta_R^N)$	$\Delta_R^N \sim P_R = 3e^{-8}$
Ω^m	$\Omega^m = \Omega + \Delta_\Omega^N$	$\Delta_\Omega^N \sim P_\Omega = 3e^{-7}$

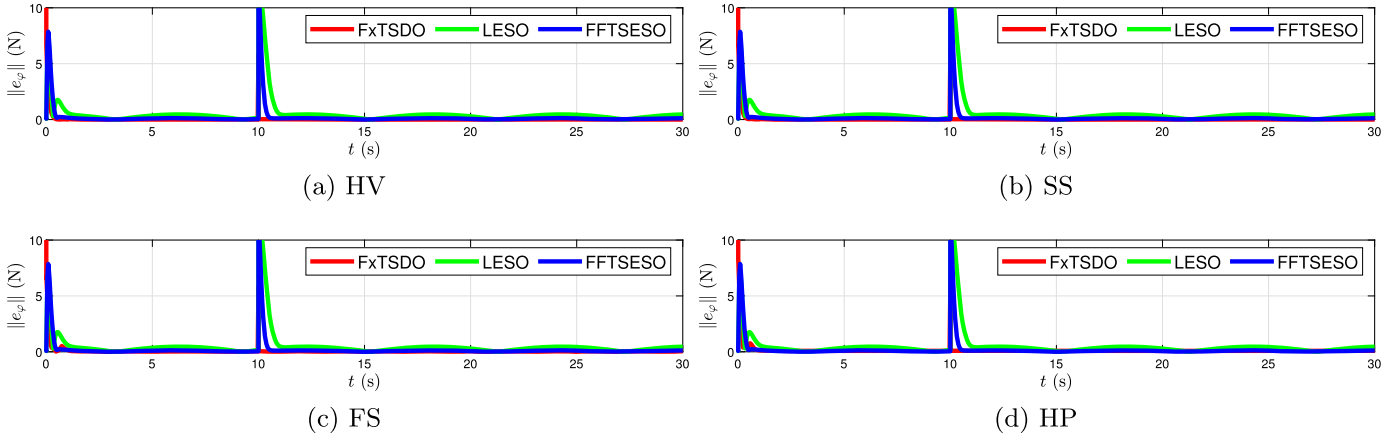

Fig. 3. Disturbance force estimation errors from FxTSDO, LESO, and FFTS-ESO, in four different trajectories without measurement noise. (For interpretation of the colors in the figure(s), the reader is referred to the web version of this article.)

The four desired flight trajectories are listed in Table 1. Hovering (HV) is the simplest flight trajectory where the aircraft is ordered to hover at a fixed position during the simulation. High pitch (HP) is the most complex flight trajectory where the aircraft has to pitch up and track a circular trajectory. Since the norm of centripetal acceleration in the HP trajectory is more than a g (gravitational acceleration), the aircraft has to flip over to track the desired trajectory. This desired trajectory with high centripetal acceleration forces the aircraft to go past the 90° pitch singularity of an Euler angle attitude representation. The measurement noise levels are as listed in Table 2 in terms of power spectral density (PSD). The disturbance force and torque in all of the four trajectories in this set of simulations are identical and are given by the following functions:

$$\varphi_D(t) = \begin{cases} [3,\ 4,\ -5]^{\mathrm{T}} + \sin\left(\frac{\pi t}{6}\right)[1.5,\ -1,\ -1]^{\mathrm{T}}\ \mathrm{N} & t < 10\ \mathrm{s} \\ [5,\ -3,\ 4]^{\mathrm{T}} + \sin\left(\frac{\pi t}{6}\right)[1.5,\ -1,\ -1]^{\mathrm{T}}\ \mathrm{N} & t \geq 10\ \mathrm{s} \end{cases},$$

$$\tau_D(t) = \begin{cases} [-0.3,\ 0.2,\ 0.2]^{\mathrm{T}} + 0.01\sin\left(\frac{\pi t}{2}\right)[1,\ 2,\ -5]^{\mathrm{T}}\ \mathrm{N\cdot m} & t < 20\ \mathrm{s} \\ [0.2,\ -0.3,\ -0.2]^{\mathrm{T}} + 0.01\sin\left(\frac{\pi t}{2}\right)[1,\ 2,\ -5]^{\mathrm{T}}\ \mathrm{N\cdot m} & t \geq 20\ \mathrm{s} \end{cases}$$

The parameters for FFTS-ESO in these simulations are $p = 1.2, k_{t1} = 3, k_{t2} = 2, k_{t3} = 6, \kappa_t = 0.8, k_{a1} = 3, k_{a2} = 2, k_{a3} = 4, \kappa_a = 0.6$. The gains for FxTSDO and LESO are as given by Liu et al. [22] and by Shao et al. [36]. In the simulated flights, the initial states of the vehicle are identical, given by: $R(0) = I,\ \Omega(0) = [0,\ 0,\ 0]^{\mathrm{T}}$ rad/s, $b(0) = [0.01,\ 0,\ 0]^{\mathrm{T}}$ m, $v(0) = [5\pi,\ 0,\ 0]^{\mathrm{T}}$ m/s. The initial conditions for the FxTSDO, LESO, and FFTS-ESO are given by the pose, velocities, and disturbances on the vehicle at the initial time in the simulations.

We present the simulation results in four sets of plots. Figs. 3 and 4 present the disturbance force and torque estimation errors respectively, from FxTSDO, LESO and FFTS-ESO in the flight trajectories described in Table 1 with noise-free measurements. Figs. 5 and 6 present the disturbance estimation errors from these schemes for the flight trajectories in Table 1, in the presence of measurement noise levels as described in Table 2.

Fig. 3 shows the disturbance force estimation errors from the three schemes with noise-free measurements. Although the disturbance force estimation error from FxTSDO shows a significant initial transient, the results from Fig. 3 indicate that with noise-free measurement, the disturbance force estimations from these three schemes converge to the origin in all four flight trajectories. The transients at $t = 10$ s are from the step-function component of disturbance force φ_D, whose step time is $t = 10$ s. Fig. 4 shows the disturbance torque estimation errors from the three schemes with noise-free measurement. In Fig. 4, we observe that when $t = 10$ s, high transients appear in the disturbance torque estimation error from FxTSDO.

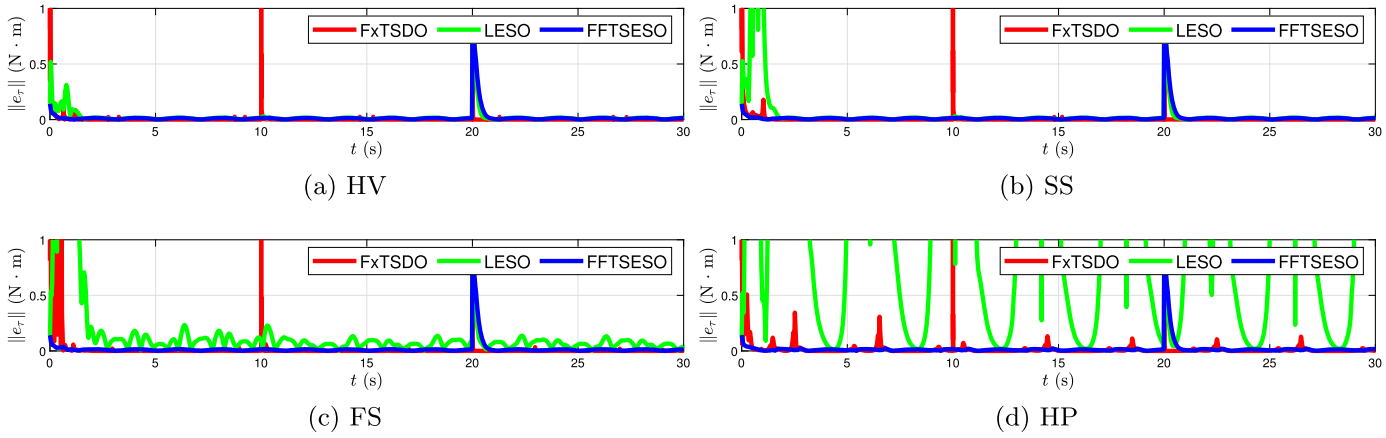

Fig. 4. Disturbance torque estimation errors from FxTSDO, LESO, and FFTS-ESO, in four different trajectories without measurement noise.

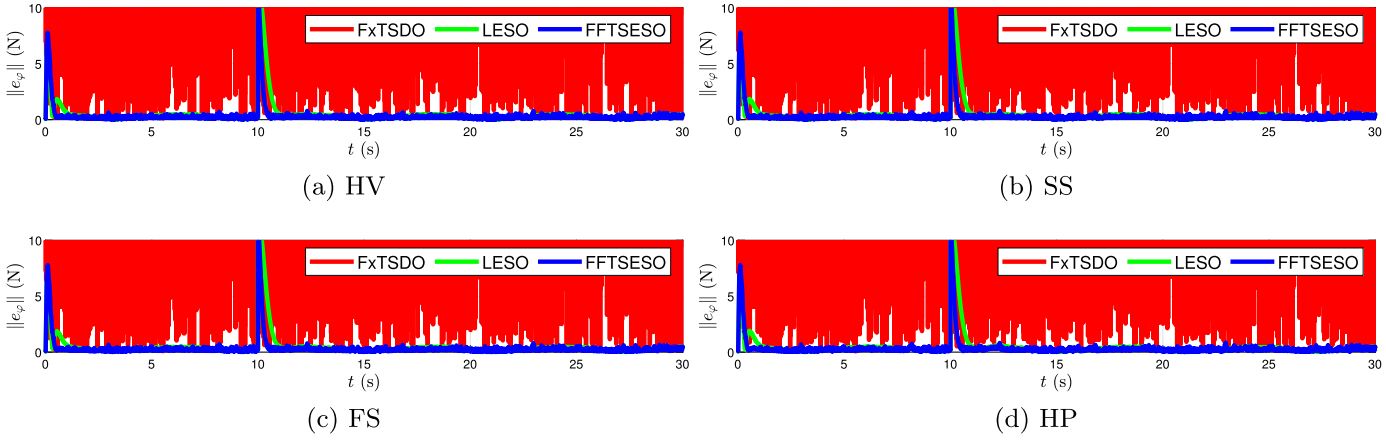

Fig. 5. Disturbance force estimation errors from FxTSDO, LESO, and FFTS-ESO, in four different trajectories with measurement noise.

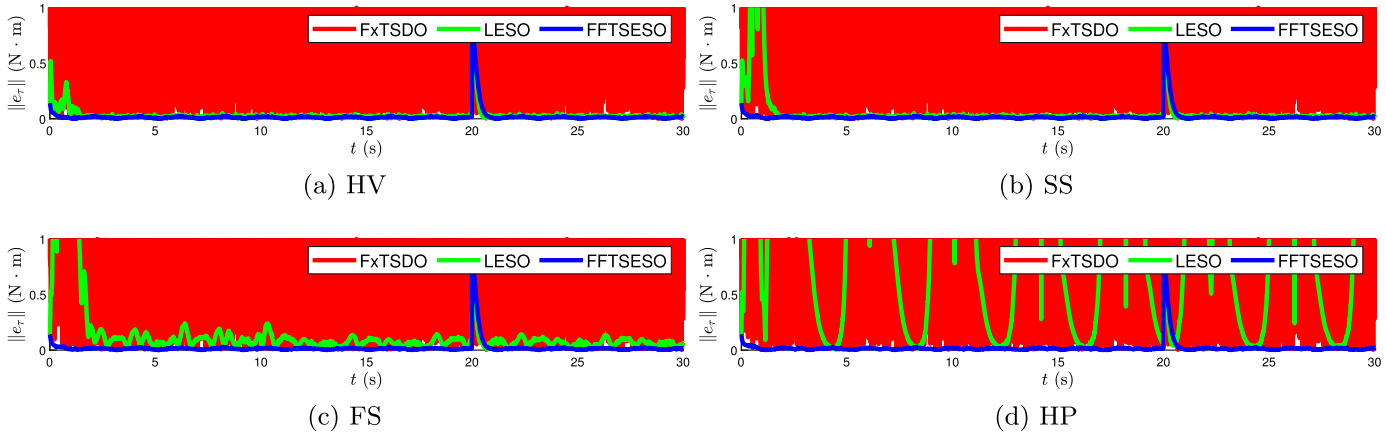

Fig. 6. Disturbance torque estimation errors from FxTSDO, LESO, and FFTS-ESO, in four different trajectories with measurement noise.

From Figs. 5 (a)-(b) and Figs. 4 (a)-(b), we observe that FxTSDO and LESO have satisfactory estimation performance with noise-free measurements in HV and SS simulations. These results indicate that the performances of FxTSDO and LESO are replicated correctly in our simulations.

Despite the initial transients, the disturbance torque estimation errors from all three schemes converge to the origin in the HV and SS simulations. However, in FS and HP simulations, the disturbance torque estimation errors from LESO and FxTSDO diverge. As is stated in Section 1, since the LESO uses Euler-angle to represent attitude for disturbance torque estimation, it experiences a singularity in attitude representation when the vehicle tracks the FS and HP trajectories. See Fig. 4 (d), the singularity in the attitude representation destabilizes the disturbance torque estimation error of LESO.

Figs. 5 and 6 present the disturbance force and disturbance torque estimation errors respectively, from the three schemes with identical noisy measurements as given in Table 2. As stated in Remark 2, we observe that with measurement noise, FxTSDO is not capable of providing any meaningful disturbance estimation. In FS and HP simulations, the disturbance torque estimation errors from LESO diverge from the origin.

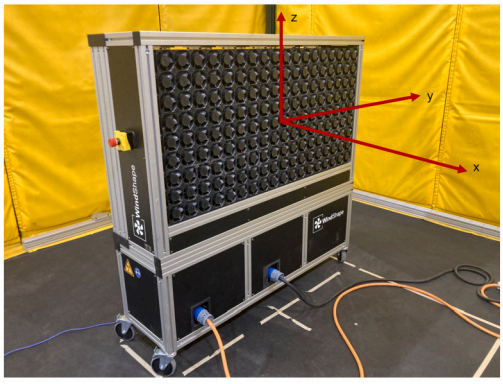

Fig. 7. The FAWT and its body-fixed coordinate frame.

Fig. 8. Quadrotor UAV developed in the autonomous unmanned system lab (AUSL) at Syracuse University.

To summarize, Figs. 3, 4, 5, and 6 show that FFTS-ESO has satisfactory disturbance estimation performance and outperforms LESO and FxTSDO when vehicle experiences large pose changes and has noisy measurements.

7. Flight experiments

In this section, the proposed FFTS-ESO is validated through flight experiments. Its hardware and software are custom-designed and developed based on the open-source autopilot PX4 by Meier et al. [25]. To demonstrate the capability of estimating and rejecting the disturbances, flight experiments are conducted under wind disturbances generated by a fan array wind tunnel (FAWT) from the Switzerland-based company WindShape. We first describe the hardware and software configurations of the multi-rotor vehicle and the setup of the experiment. Afterwards, we present our experimental results including the characteristics of the wind disturbances and the control performance of the vehicle when exposed to disturbances generated by the FAWT.

7.1. Hardware configuration

The multi-rotor vehicle is shown in Fig. 8. It has four brushless direct current electrical motors (T-Motor Air 2216 880-KV) paired with $10'' \times 4.5''$ carbon fiber propellers. To control the rotational speed of the motors, each is connected to an electronic speed control (T-Motor Air 20A), which receives commands from a PixHawk flight control unit (FCU, CUAV Nora plus) with redundant inertial measurement units (IMU). Flight control and state estimation are conducted by the FCU. The pose of the vehicle is measured by an optical motion capture system (VICON), and is sent to a companion computer (Raspberry Pi 4) through a Wi-Fi network, and then passed on to the FCU through a telemetry port. To generate wind fields with various turbulence characteristics for the flight experiments, we leveraged the FAWT in Fig. 7. The wind tunnel is a 1.44 m by 0.72 m array of 162 independently controllable fans capable of generating wind speeds up to 12 m/s. The distributed fans are controlled in real time by a Python program. In our flight experiments, the FAWT was run at the steady uniform flow mode, with each individual fan running at identical and constant duty.

7.2. Software configuration

The flight control software is developed from the open-source autopilot software PX4 v1.13.2. According to [25], the system architecture of PX4 is centered around a publish-subscribe object request broker on top of a POSIX application programming interface. This programming interface has different modules for data logging, communication, estimation, and control. The original control scheme of PX4 is a cascaded proportional-integral-derivative scheme to track the desired trajectory, which is denoted by $g^d(t) = (b^d, R^d) \in \mathrm{SE}(3)$. To indicate the control performance, we denote the tracking error by

$$(b^e, R^e) \in \mathrm{SE}(3), \tag{88}$$

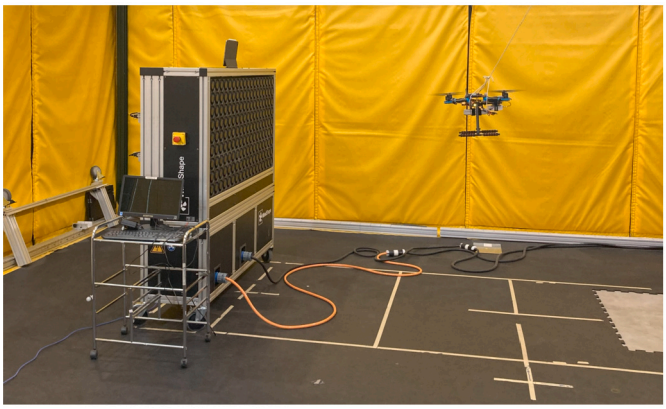

Fig. 9. Setup for our flight control experiments.

where $R^e = (R^d)^{\mathrm{T}} R^m$ is the attitude tracking error in frame $\mathcal{B}$, and $b^e = b^m - b^d$ is the position tracking error in frame $\mathcal{E}$. The FFTS-ESO is implemented onto the modules `mc_pos_control` and `mc_rate_control` for translational and rotational motions, respectively. The feedback of disturbance estimates from the FFTS-ESO is applied to the control law as an additional term so that the original control architecture is modified with this feedforward disturbance rejection term. This implemented control law is given by

$$F = F_0 - \hat{\varphi}_D, \quad \tau = \tau_0 - \hat{\tau}_D,$$

where $F, \tau \in \mathbb{R}^3$ are commanded force and torque in the flight control system respectively, F_0, τ_0 are the baseline control law provided by PX4, and $\hat{\varphi}_D, \hat{\tau}_D$ are estimated disturbances from the implemented FFTS-ESO. Boolean parameters are introduced in the control law to switch on the disturbance rejection terms.

In the experiment, the rest of the autopilot (PX4 v1.13.2) is kept unchanged, to make a fair comparison of flight control performance between the original PX4 autopilot, and the one with disturbance rejection from FFTS-ESO. The flight control parameters of the autopilot are as described in the multi-rotor frame S500 in https://github.com/PX4/PX4-Autopilot/. A Robot Operating System (ROS) interface program is developed for the companion computer that transmits commands and poses to the vehicle. The flight data are saved in the memory card inside the FCU in the form of .ulg file for post-processing. We use the MAVLINK telecommunication protocol for communication between the FCU, companion computer, and ground control station.

The FFTS-ESO parameters are selected as: $p = 1.2, k_{t1} = 6, k_{t2} = 3, k_{t3} = 1, \kappa_t = 0.6$, $k_{a1} = 8, k_{a2} = 4, k_{a3} = 2, \kappa_a = 0.6$. The empirically known mass and inertia of the vehicle as given to the FFTS-ESO are: $m = 1$ kg and $J = \mathrm{diag}([0.03, 0.03, 0.06])$ kg $\cdot$ m^2.

7.3. Experiment procedure

The flight experiment setup is shown in Fig. 9. We define the FAWT coordinate frame as shown in Fig. 7, with x as the stream-wise direction, y as the span-wise direction, and z as the vertically up direction. The origin is at the geometric center of the fan array. We operated the FAWT at a steady uniform flow mode at 30%-70% of its maximum duty to measure the wind velocity of the wind field. We carried out wind velocity measurements with a hotwire anemometer facing in the x direction at $x = 1.2$ m, $y = 0$ m, $z = 0$ m in the FAWT coordinate system.

As shown in Fig. 9, the vehicle was commanded to hover in the front of the FAWT, at $x = 1.5$ m, $y = 0$ m, $z = 0$ m in the FAWT frame. The pose of the vehicle during flight was recorded in the log file for evaluation. This hovering position was at the center point of the test section so that we could maximally avoid the boundary layer around the section border, where higher turbulence intensity and flow uncertainty occur. The time for hovering flight was set to 210 s. During this period, we turned on the FAWT for 150 s to disturb the vehicle with turbulent flows with statistically constant characteristics. The flight experiment procedure is available as a video.[1] In this video, the vehicle took off at 20 s and moved to the hovering position at around 30 s. The FAWT was turned on at 40 s and turned off at 200 s, when large transient motions of the vehicle can be observed. The vehicle landed after 250 s.

7.4. Results: turbulent flow measurement

The results for hot-wire measurements are covered in this subsection. For brevity, we omit the details of the measurement procedure. According to the Reynolds decomposition given in [30], we decompose the measured wind velocity u_i into the sum of a time-averaged velocity U_i and fluctuating velocity u_i', such that $u_i = U_i + u_i'$. Based on hotwire measurements, we characterize the FAWT wind field with the following quantities: time-averaged velocity U_i, variance of the fluctuating velocity $\overline{(u_i')^2}$, Taylor-microscale Reynolds number Re_λ, and turbulence intensity (TI). Re_λ is the Reynolds number calculated based on the Taylor microscale [30], which indicates the length scale at which fluid viscosity significantly affects the dynamics of turbulent eddies in the flow. TI is defined by $\sqrt{\overline{(u_i')^2}}/U_i$, which is the ratio of the root mean square of fluctuating velocity and the time-averaged velocity (Table 3).

To summarize, for the FAWT in the setup described earlier in this subsection, we observe that U_i ranges from 5.472 m/s to 10.920 m/s, and TI is around 0.043. Moreover, we observe that $\overline{(u_i')^2}$ has a positive correlation with U_i. We assume that higher $\overline{(u_i')^2}$ brings higher turbulence energy, which causes higher disturbance inputs to the multi-rotor vehicle flying within the wind field.

[1] https://1drv.ms/v/s!AkzQytNDIPfpnuVPMgVduKJMLuS2TQ?e=9HZmvj.

Table 3
Turbulence characteristics of uniform flows.

Duty	U_i (m/s)	$\overline{u_i' u_i'}$ (m/s)^2	Re_λ	TI
30%	5.472	0.061	98	0.0451
40%	6.876	0.082	102	0.0417
50%	8.213	0.116	100	0.0415
60%	9.590	0.168	127	0.0427
70%	10.920	0.237	148	0.0446

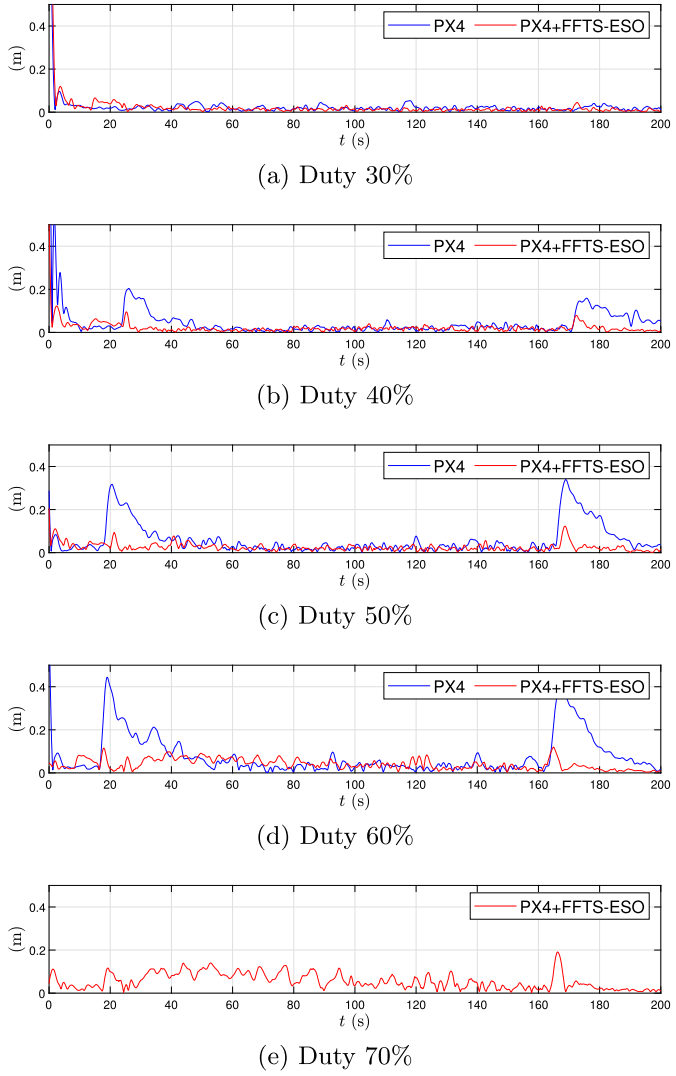

Fig. 10. Position tracking error.

7.5. Results: flight experiment

The results of the flight experiment are covered in this subsection. Fig. 10 and Fig. 11 illustrate the position and attitude tracking errors defined by (88). The position tracking error b^e is expressed through its Euclidean norm, while the attitude tracking error R^e is quantified by its principal angle, given by $\Phi = \mathrm{acos}\left(\frac{\mathrm{tr}(R^e)-1}{2}\right)$. To highlight the flight control performance under disturbances, we omit the pose data during take-off and landing in the results presented. Results for the control scheme without disturbance rejection are plotted in blue, and those with disturbance rejection are in red. The time-averaged position and attitude tracking errors are listed in Table 4.

Figs. 10 and 11 show that both position and attitude tracking errors have high transients at around 20 s and 180 s when disturbances from the FAWT kick in and turn off, respectively. Fig. 11 for the attitude tracking error of the control scheme with disturbance rejection shows an extra transient at around 0-10 s when the disturbance rejection kicks in. In Fig. 10, we observe that when the FAWT operates at 40%-60% of its maximum duty, the position tracking error of the control scheme with disturbance rejection outperforms the one without rejection. When the FAWT operates at 30% of its maximum duty, the difference between the two control schemes is not evident in Fig. 10. However, in terms of the time-averaged position tracking errors in Table 4, we can still observe that the scheme with disturbance rejection outperforms the one without rejection when the

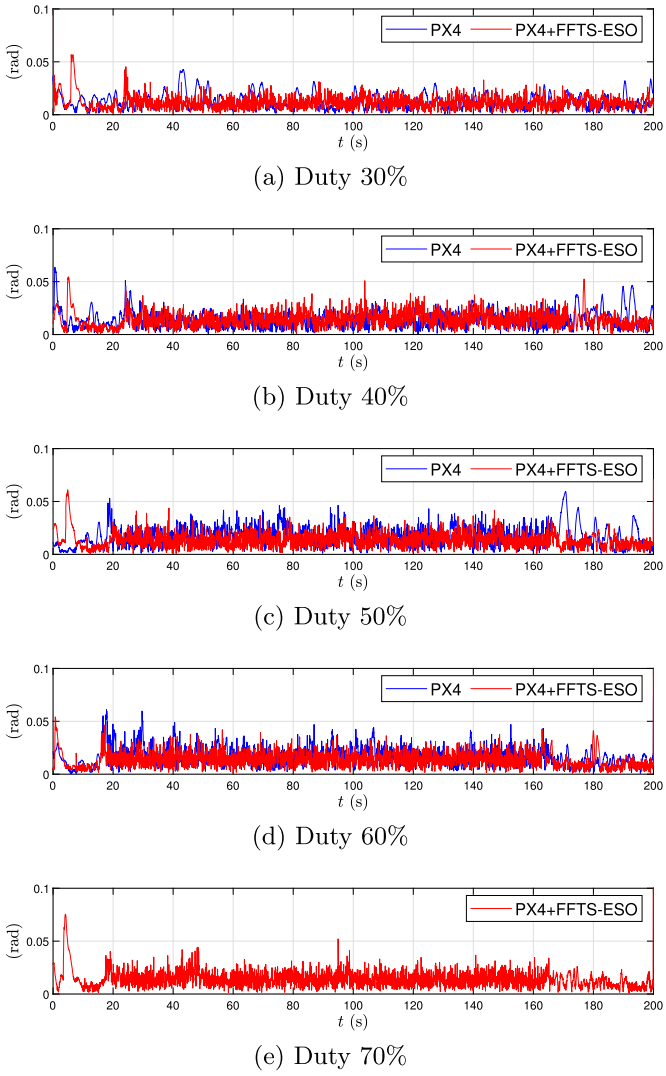

Fig. 11. Attitude tracking error.

Table 4
Time-averaged tracking error.

	Position tracking error (m)		Attitude tracking error (rad)	
	PX4	PX4+FFTS-ESO	PX4	PX4+FFTS-ESO
30%	0.0251	0.0236	0.0125	0.0116
40%	0.0468	0.0211	0.0140	0.0141
50%	0.0589	0.0254	0.0166	0.0132
60%	0.0792	0.0400	0.0164	0.0134
70%	Failed!	0.0557	Failed!	0.0139

FAWT operates at 30%-60% of its maximum duty. When the FAWT operates at 70% of its maximum duty, the control scheme without disturbance rejection fails to make the UAV hover in a stable manner, while the one with rejection succeeds in doing so.

8. Conclusion

In this article, a FFTS-ESO scheme for disturbance estimation is designed for multi-rotor vehicles with a body-fixed thrust direction and three-axis attitude control. The vehicle is modeled as an under-actuated system on the state-space TSE(3), the tangent bundle of the six-dimensional Lie group SE(3). The ESO scheme is developed based on the HC-FFTSD, which is similar to the STA used in sliding mode designs, to obtain fast finite-time stability with higher tunability of the settling time compared to other FTS schemes. A Lyapunov stability analysis of this ESO scheme proves its finite-time stability and robustness on TSE(3). A set of numerical simulations are conducted. The numerical simulation results show the stable performance of the FFTS-ESO scheme in estimating external force and torque disturbances acting on the vehicle in different trajectories. The behavior of the FFTS-ESO is compared with two state-of-the-art observers (LESO and FxTSDO) for disturbance estimation, using a realistic set of data for several simulated flight trajectories of a multi-rotor vehicle. These numerical simulations show that the FFTS-ESO, unlike the LESO and FxTSDO, is always stable and its convergence is robust to measurement noise and pose singularities. The FFTS-ESO is implemented on the FCU of a multi-rotor

vehicle, with disturbance rejection control using feedback of disturbance estimates from this FFTS-ESO. The results validate the performance of this FFTS-ESO experimentally and demonstrate its robust disturbance rejection capabilities in comparison to the original control scheme.

CRediT authorship contribution statement

Ningshan Wang: Writing – review & editing, Writing – original draft, Visualization, Validation, Software, Methodology, Investigation, Formal analysis. **Reza Hamrah:** Writing – review & editing, Validation, Investigation. **Amit K. Sanyal:** Writing – review & editing, Writing – original draft, Supervision, Project administration, Methodology, Funding acquisition, Conceptualization. **Mark N. Glauser:** Writing – review & editing, Supervision, Resources, Project administration.

Declaration of competing interest

The authors declare the following financial interests/personal relationships which may be considered as potential competing interests: Ningshan Wang reports financial support was provided by National Science Foundation. Amit K. Sanyal reports financial support was provided by National Science Foundation. If there are other authors, they declare that they have no known competing financial interests or personal relationships that could have appeared to influence the work reported in this paper.

Data availability

Codes and video have been shared through links provided in the manuscript.

References

[1] M. Bangura, R. Mahony, Thrust control for multirotor aerial vehicles, IEEE Trans. Robot. 33 (2) (2017) 390–405.
[2] P. Bhale, M. Kumar, A.K. Sanyal, Finite-time stable disturbance observer for unmanned aerial vehicles, in: American Control Conference (ACC) 2022, 2022, pp. 5010–5015.
[3] S.P. Bhat, D.S. Bernstein, Finite-time stability of continuous autonomous systems, SIAM J. Control Optim. 38 (3) (2000) 751–766.
[4] S.P. Bhat, D.S. Bernstein, A topological obstruction to continuous global stabilization of rotational motion and the unwinding phenomenon, Syst. Control Lett. 39 (1) (2000) 63–70.
[5] M. Bisheban, T. Lee, Geometric adaptive control with neural networks for a quadrotor in wind fields, IEEE Trans. Control Syst. Technol. 29 (4) (2020) 1533–1548.
[6] J. Bohn, A.K. Sanyal, Almost global finite-time stabilization of rigid body attitude dynamics using rotation matrices, Int. J. Robust Nonlinear Control 26 (9) (2016) 2008–2022.
[7] N.A. Chaturvedi, A.K. Sanyal, N.H. McClamroch, Rigid-body attitude control, IEEE Control Syst. Mag. 31 (3) (2011) 30–51.
[8] C.-T. Chen, Linear System Theory and Design, Saunders College Publishing, 1984.
[9] W.-H. Chen, Nonlinear disturbance observer-enhanced dynamic inversion control of missiles, J. Guid. Control Dyn. 26 (1) (2003) 161–166.
[10] W. Craig, D. Yeo, D.A. Paley, Geometric attitude and position control of a quadrotor in wind, J. Guid. Control Dyn. (2020) 1–14.
[11] L. Cui, R. Zhang, H. Yang, Z. Zuo, Adaptive super-twisting trajectory tracking control for an unmanned aerial vehicle under gust winds, Aerosp. Sci. Technol. 115 (2021) 106833.
[12] M. Faessler, A. Franchi, D. Scaramuzza, Differential flatness of quadrotor dynamics subject to rotor drag for accurate tracking of high-speed trajectories, IEEE Robot. Autom. Lett. 3 (2) (2017) 620–626.
[13] B.-Z. Guo, Z.-l. Zhao, On the convergence of an extended state observer for nonlinear systems with uncertainty, Syst. Control Lett. 60 (6) (2011) 420–430.
[14] D. Hanover, P. Foehn, S. Sun, E. Kaufmann, D. Scaramuzza, Performance, precision, and payloads: adaptive nonlinear mpc for quadrotors, IEEE Robot. Autom. Lett. 7 (2) (2021) 690–697.
[15] G.H. Hardy, J.E. Littlewood, G. Pólya, G. Pólya, et al., Inequalities, Cambridge University Press, 1952.
[16] R.J. Hartlieb, The cancellation of random disturbances in automatic control systems, Ph.D. Thesis, 1956.
[17] Y. Huang, K. Xu, J. Han, J. Lam, Flight control design using extended state observer and non-smooth feedback, in: Proceedings of the 40th IEEE Conference on Decision and Control (Cat. No. 01CH37228), vol. 1, 2001, pp. 223–228.
[18] J. Jia, K. Guo, X. Yu, W. Zhao, L. Guo, Accurate high-maneuvering trajectory tracking for quadrotors: a drag utilization method, IEEE Robot. Autom. Lett. 7 (3) (2022) 6966–6973.
[19] H.K. Khalil, Nonlinear Systems, third edition, Patience Hall, 2002, p. 115.
[20] T. Lee, M. Leok, N.H. McClamroch, Geometric tracking control of a quadrotor UAV on SE(3), in: 49th IEEE Conference on Decision and Control (CDC), 2010, pp. 5420–5425.
[21] X. Liang, B. Xu, R. Hong, M. Sang, Quaternion observer-based sliding mode attitude fault-tolerant control for the reusable launch vehicle during reentry stage, Aerosp. Sci. Technol. 129 (2022) 107855.
[22] K. Liu, R. Wang, S. Zheng, S. Dong, G. Sun, Fixed-time disturbance observer-based robust fault-tolerant tracking control for uncertain quadrotor UAV subject to input delay, Nonlinear Dyn. 107 (3) (2022) 2363–2390.
[23] L. Liu, D. Wang, Z. Peng, State recovery and disturbance estimation of unmanned surface vehicles based on nonlinear extended state observers, Ocean Eng. 171 (2019) 625–632.
[24] O. Mechali, L. Xu, Y. Huang, M. Shi, X. Xie, Observer-based fixed-time continuous nonsingular terminal sliding mode control of quadrotor aircraft under uncertainties and disturbances for robust trajectory tracking: theory and experiment, Control Eng. Pract. 111 (2021) 104806.
[25] L. Meier, D. Honegger, M. Pollefeys, Px4: a node-based multithreaded open source robotics framework for deeply embedded platforms, in: 2015 IEEE International Conference on Robotics and Automation (ICRA), IEEE, 2015, pp. 6235–6240.
[26] A. Moeini, A.F. Lynch, Q. Zhao, Exponentially stable motion control for multirotor UAVs with rotor drag and disturbance compensation, J. Intell. Robot. Syst. 103 (1) (2021) 1–17.
[27] J.A. Moreno, M. Osorio, Strict Lyapunov functions for the super-twisting algorithm, IEEE Trans. Autom. Control 57 (4) (2012) 1035–1040.
[28] J.A. Moreno, H. Ríos, L. Ovalle, L. Fridman, Multivariable super-twisting algorithm for systems with uncertain input matrix and perturbations, IEEE Trans. Autom. Control 67 (12) (2021) 6716–6722.
[29] R.M. Murray, Z. Li, S.S. Sastry, A Mathematical Introduction to Robotic Manipulation, CRC Press, 2017.
[30] S.B. Pope, Turbulent Flows, Cambridge University Press, 2000.
[31] P. Pounds, R. Mahony, P. Corke, Modelling and control of a large quadrotor robot, Control Eng. Pract. 18 (7) (2010) 691–699.
[32] L. Rosier, Homogeneous Lyapunov function for homogeneous continuous vector field, Syst. Control Lett. 19 (6) (1992) 467–473.
[33] A. Sanyal, Discrete-time data-driven control with Hölder-continuous real-time learning, Int. J. Control 95 (8) (2022) 2175–2187.
[34] A. Sanyal, N. Nordkvist, M. Chyba, An almost global tracking control scheme for maneuverable autonomous vehicles and its discretization, IEEE Trans. Autom. Control 56 (2) (2010) 457–462.
[35] A.K. Sanyal, J. Bohn, Finite-time stabilisation of simple mechanical systems using continuous feedback, Int. J. Control 88 (4) (2015) 783–791.
[36] X. Shao, J. Liu, H. Cao, C. Shen, H. Wang, Robust dynamic surface trajectory tracking control for a quadrotor UAV via extended state observer, Int. J. Robust Nonlinear Control 28 (7) (2018) 2700–2719.
[37] G. Torrente, E. Kaufmann, P. Föhn, D. Scaramuzza, Data-driven mpc for quadrotors, IEEE Robot. Autom. Lett. 6 (2) (2021) 3769–3776.
[38] P.V. Vidal, E.V. Nunes, L. Hsu, Output-feedback multivariable global variable gain super-twisting algorithm, IEEE Trans. Autom. Control 62 (6) (2016) 2999–3005.
[39] S.P. Viswanathan, A.K. Sanyal, E. Samiei, Integrated guidance and feedback control of underactuated robotics system in SE(3), J. Intell. Robot. Syst. 89 (1) (2018) 251–263.
[40] S.P. Viswanathan, A.K. Sanyal, R.R. Warier, Finite-time stable tracking control for a class of underactuated aerial vehicles SE(3), in: 2017 American Control Conference (ACC), 2017, pp. 3926–3931.
[41] N. Wang, A.K. Sanyal, A Hölder-continuous extended state observer for model-free position tracking control, in: 2021 American Control Conference (ACC), IEEE, 2021, pp. 2133–2138.

[42] N. Wang, A.K. Sanyal, A Hölder-continuous extended state observer for rigid body attitude dynamics, IFAC-PapersOnLine 55 (22) (2022) 340–345.
[43] Y. Xia, Z. Zhu, M. Fu, S. Wang, Attitude tracking of rigid spacecraft with bounded disturbances, IEEE Trans. Ind. Electron. 58 (2) (2010) 647–659.
[44] J. Yu, P. Shi, L. Zhao, Finite-time command filtered backstepping control for a class of nonlinear systems, Automatica 92 (2018) 173–180.
[45] S. Yu, X. Yu, B. Shirinzadeh, Z. Man, Continuous finite-time control for robotic manipulators with terminal sliding mode, Automatica 41 (11) (2005) 1957–1964.
[46] Z. Zhu, Y. Xia, M. Fu, Attitude stabilization of rigid spacecraft with finite-time convergence, Int. J. Robust Nonlinear Control 21 (6) (2011) 686–702.